Vibrational echoes: a new approach to condensed-matter vibrational spectroscopy

by K. D. RECTOR and M. D. FAYER

Department of Chemistry, Stanford University, Stanford, CA 94305, USA

This review describes the first ultrafast infrared vibrational echo experiments, which are used to examine liquids, glasses and proteins. Like the nuclear magnetic resonance (NMR) spin echo and other NMR pulse sequences, the vibrational echo can extract dynamical and spectroscopic information that cannot be obtained from a vibrational absorption spectrum. The vibrational echo measures the homogeneous vibrational linewidth even if the absorption line is massively inhomogeneously broadened. When combined with pump–probe (transient absorption) experiments, the homogeneous pure dephasing (energy level fluctuations) is obtained. Conducting these experiments as a function of temperature provides information on dynamics and intermolecular interactions. The nature of the method and the experimental procedures are outlined. Experimental results are presented for the metal carbonyl solutes, $W(CO)_6$ and $Rh(CO)_2acac$, in several glassy and liquid solvents. The dynamics of the CO ligand bound at the active site of the protein myoglobin are examined and compared with those in several myoglobin mutants. The results provide insights into protein dynamics and how protein structural fluctuations are communicated to a ligand bound at the active site. In addition, two new vibrational echo methods are reviewed. One method involves using multilevel vibrational coherences, which gives rise to vibrational echo beats, to measure vibrational anharmonicities and excited-state dephasing. The other method, in which a vibrational echo spectrum is taken, is demonstrated to be capable of the suppression of unwanted background that dominates the normal vibrational absorption spectrum.

1. Introduction

A molecule in a condensed-matter system, such as a liquid, glass or protein, is influenced by intermolecular interactions with the surrounding medium. The average force exerted by the solvent on a molecular oscillator causes a static shift in the vibrational absorption frequency. The frequency shift in going from the gas phase to a condensed-matter environment is an indicator of the effect of the solvent on the internal mechanical degrees of freedom of a solute.

The medium also exerts fluctuating forces on the solute molecule, producing fluctuations in molecular structure, time-dependent vibrational eigenstates and, thus, time-dependent vibrational energy eigenvalues. Fluctuating forces are involved in a wide variety of chemical and physical phenomena, including thermally induced chemical reactions, promotion of a molecule to a transition state, electron transfer, and energy flow into and out of molecular vibrations. Fluctuations of the vibrational energy levels are sensitive to the nature of the dynamics of the condensed-matter environment and the strength of intermolecular interactions. Time evolution of the vibrational energy eigenvalues gives rise to fluctuations in vibrational energy level separations, that is the vibrational transition energy. The bath, which gives rise to the fluctuating forces responsible for the time evolution of the vibrational transition energy and other vibrational dynamics, includes bulk solvent degrees of freedom arising from the solvent molecule's translational and orientational motions, the

internal vibrational degrees of freedom of the solvent, and the solute's vibrational modes other than the oscillator of interest.

In a glass, bath fluctuations range from very high frequency to essentially static. For a pair of energy levels, for example $v = 0$ and $v = 1$, the fast fluctuations produce homogeneous pure dephasing which, in the frequency domain, is a cause of homogeneous spectral broadening. Pure dephasing results from the time evolution of the vibrational transition energy. Compared with a fixed-frequency clock running at the centre frequency of a vibrational transition, fluctuations of the vibrational transition frequency about the average cause a vibrational oscillator to lose its well defined phase relationship with the clock. The members of an ensemble of oscillators will lose their phase relationship with the clock and with each other. Therefore, pure dephasing is an ensemble-averaged property, which for an exponential decay of the off-diagonal density matrix elements (Lorentzian homogeneous line shape) can be characterized by an ensemble-average pure dephasing time T_2^*. The total homogeneous dephasing time T_2 (total homogeneous linewidth) also has contributions from the vibrational lifetime T_1.

Evolution of the system on time scales substantially slower than T_2 appear as inhomogeneous broadening. If the inhomogeneous broadening is large compared with the homogeneous broadening, an absorption spectrum will measure the inhomogeneous linewidth, which does not provide information on vibrational dynamics. In a glass, the time scale of the slowest system evolution may be so long that there is truly static inhomogeneous broadening. However, there are also slow fluctuations that do not contribute to homogeneous pure dephasing but give rise to spectral diffusion, that is slow evolution of the transition frequency. Spectral diffusion has been observed in electronic excitation dephasing experiments in glasses [1–3] and has also been observed for vibrational transitions [4, 5]. A protein at low temperatures (below about 100 K) will also have degrees of freedom that are essentially static on any experimentally accessible time scale and, like a glass, have distinct homogeneous and static inhomogeneous linewidths.

Dephasing in proteins at high temperatures (greater than about 200 K) or in liquids is similar to but not identical with the situation in low-temperature glasses. There is a range of high-frequency fluctuations that give rise to homogeneous pure dephasing. Compared with this time scale, there can be inhomogeneous broadening arising from more slowly evolving components of the liquid or protein structure. However, unlike a glass, essentially static local environments that give rise to permanent inhomogeneous broadening do not exist. In liquids, and probably in room-temperature proteins, spectral diffusion will cause all possible transition energies to be sampled by an oscillator on a relatively short time scale.

In principle, information on dynamical intermolecular interactions of an oscillator with its environment can be obtained from vibrational absorption spectra. The forces experienced by the oscillator determine the vibrational line shape and linewidth. The line shape and linewidth depend on temperature and the nature of the solvent. However, a vibrational absorption spectrum reflects the full range of broadening of the vibrational transition energies, both homogeneous and inhomogeneous. In glasses, liquids and proteins, inhomogeneous broadening often exceeds the homogeneous linewidth. Under these circumstances, measurement of the absorption spectrum does not provide information on vibrational dynamics.

The ultrafast infrared (IR) vibrational echo experiment, which is the vibrational equivalent of the magnetic resonance spin echo [6] and the electronic excitation photon
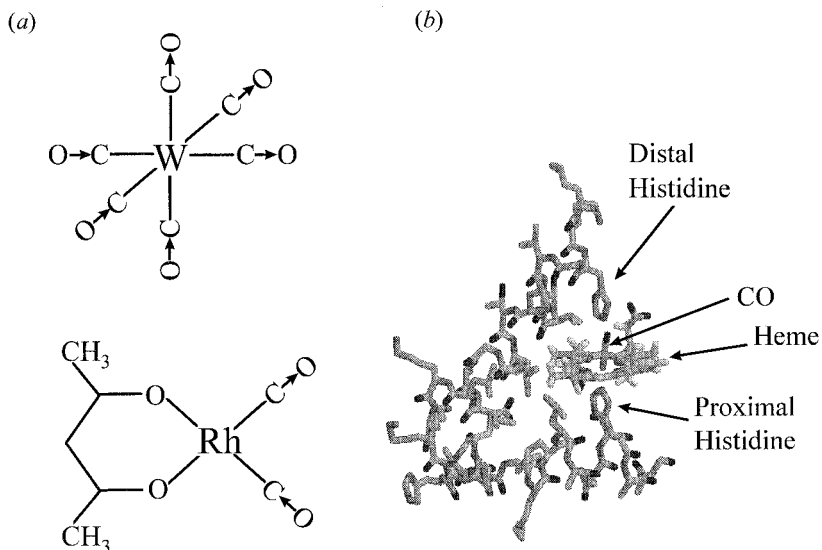
(*a*)   (*b*)

Figure 1.   (*a*) Chemical structures of $W(CO)_6$ and $Rh(CO)_2acac$. The modes studied are the asymmetric CO stretch modes which are near 5 μm. (*b*) Structure of Mb–CO near the haem pocket. The CO is bound to the Fe of the haem. Two important amino acids are the proximal histidine (position 93, only covalent link between the haem and the globin) and the distal histidine (position 64, closest non-bonded polar amino acid to the CO).

echo [7, 8], eliminates the inhomogeneous broadening contribution to the linewidth and provides a direct measurement of homogeneous dephasing (homogeneous spectrum). Using vibrational echoes to measure the homogeneous dephasing time T_2 and IR pump–probe experiments to measure the vibrational lifetime T_1 (and orientational relaxation if it occurs), the homogeneous pure dephasing time T_2^* can be obtained. Thus, by using nonlinear vibrational experiments in the time domain, it is possible to determine the homogeneous spectrum and all dynamical contributions to it.

In this article, the first applications of ultrafast vibrational echo experiments to the study of dynamics in condensed-matter systems are reviewed. In addition to vibrational echo experiments, associated vibrational pump–probe experiments are described. In all the experiments discussed here, CO stretching modes of metal carbonyls were studied. Comprehensive studies of two molecules, (acetylacetonato)-dicarbonylrhodium(I) [$Rh(CO)_2acac$] and tungsten hexacarbonyl [$W(CO)_6$] (figure 1(*a*)) are described. The vibrational echo and pump–probe experiments were conducted on the asymmetric CO stretching modes (about 2000 cm^{-1}) in several solvents as a function of temperature. The experiments were performed in room-temperature liquids, and experiments were conducted as the temperature was lowered through the glass transition down to a few kelvin, where the solvents are low-temperature glasses. In addition, studies were performed on the stretching mode of CO bound to the active site of the protein myoglobin (Mb) (figure 1(*b*)) as well as on a number of mutant Mbs. The experiments on the proteins were also conducted from room temperature to very low temperatures.

Vibrational echo experiments on $Rh(CO)_2acac$ in dibutyl phthalate (DBP) reveal that pure dephasing of the CO asymmetric stretching mode is dominated by glass structural dynamics at very low temperatures and at higher temperatures by coupling

to the low-frequency Rh–C stretching mode through modulation of back bonding interactions. Pure dephasing measurements on $W(CO)_6$ in DBP as well as in 2-methylpentane (2MP) and 2-methyltetrahydrofuran (2MTHF) demonstrate the importance of the threefold degeneracy of the asymmetric stretching mode studied in this molecule. Small splittings of the normally degenerate mode, which arise from the anisotropy of the solvent environments, enable distinct mechanisms for dephasing that are not available to the non-degenerate CO mode of $Rh(CO)_2acac$. Experiments on Mb and related compounds examine the mechanism by which protein fluctuations are communicated to the CO ligand bound at the active site of the protein. The temperature dependence demonstrates that there is a change in the nature of the protein dynamics below room temperature (about 200 K). In addition to studies of vibrational dephasing using vibrational echo experiments, an experiment that displays beats on the vibrational echo decay is shown to measure vibrational anharmonicities directly, and a method for measuring a vibrational spectrum while suppressing a broad, highly absorbing background is demonstrated. The combined work illustrates the development of the vibrational echo technique as an important new approach to the study of molecular vibrations.

This paper is outlined as follows. Section 2 details the vibrational echo technique and the experimental parameters and procedures as well as the various sample preparations. Section 3 describes the temperature-dependent vibrational pure dephasing of the CO asymmetric stretching modes of $Rh(CO)_2acac$ in DBP and $W(CO)_6$ in 2MP, DBP and 2MTHF. Section 4 discusses non-exponential decays and vibrational echo beat (VEB) spectroscopy. Discussions of the Mb protein dephasing including mutant myoglobin studies are presented in section 5. In section 6, the technique for obtaining a vibrational echo spectrum is illustrated. Some concluding remarks are made in section 7.

2. The vibrational echo method and experimental procedures
2.1. *The vibrational echo method*

The vibrational echo experiment is a time-domain degenerate four-wave mixing experiment that extracts the homogeneous vibrational line shape even from a massively inhomogeneously broadened line. Vibrational line shapes in condensed phases contain the details of the dynamic interactions of a normal mode with its environment [9–11]. However, the vibrational line shape can also include low-frequency structural perturbations associated with the distribution of the vibrational oscillator's local environmental configurations, that is inhomogeneous broadening. Thus, the vibrational echo makes it possible to extract information that cannot be obtained from an absorption spectrum.

The echo method was originally developed as the spin echo in nuclear magnetic resonance (NMR) in 1950 [6]. In 1964, the technique was extended into optical frequencies for electronic transitions as the photon echo [7, 8]. Since then, photon echoes have been used extensively to study electronic excited-state dynamics in many condensed-matter systems [3, 12–14].

The vibrational echo experiments permit the use of optical coherence methods to study the dynamics of the mechanical degrees of freedom of condensed-phase systems from low temperatures (about 3 K) to high temperatures (about 300 K). Because vibrational spectroscopic lines are relatively narrow, it is possible to perform vibrational echo experiments on well defined transitions and at temperatures which
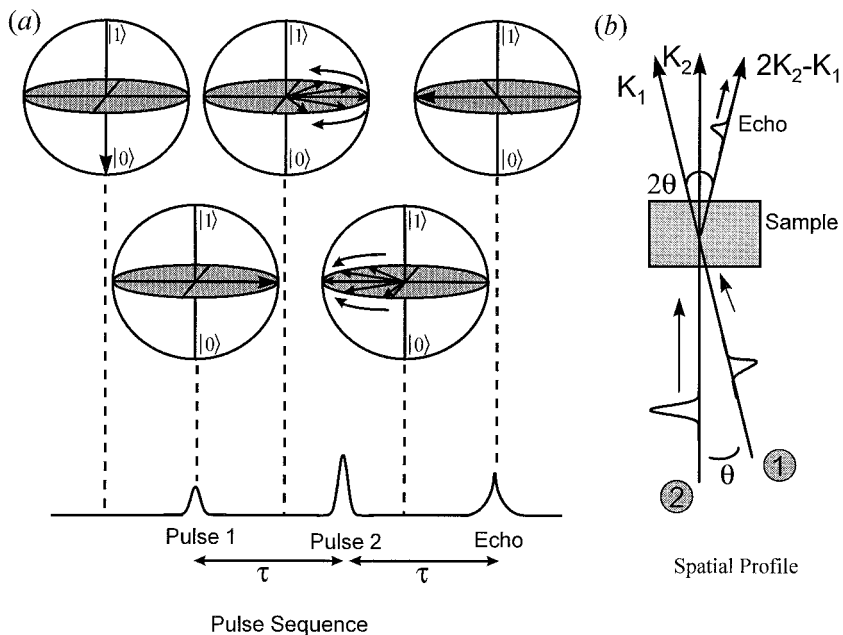
Figure 2. (*a*) Semiclassical Bloch picture of an vibrational echo in a frame rotating at the centre frequency of the vibrational line. The vertical axis in the circles represents the population axis between $|0\rangle$ and $|1\rangle$. The other two axes represent the coherence plane. Before $t = 0$, all the population is in the ground state (arrow pointing down). The first pulse shifts the molecules into the coherence plane. At this point all the molecules are in phase (single arrow pointing to the right). However, owing to homogeneous and inhomogeneous spread in vibrational frequencies, the molecules will precess at different frequencies, causing dephasing (arrows spread out in plane). After a time τ, the second pulse initiates a rephasing process (arrows come together in plane) that causes all the microscopic dipoles to rephase at 2τ (single arrow pointing to the left). The arrow pointing to the left represents, in the laboratory frame, a macroscopic dipole that radiates the vibrational echo. (*b*) Spatial profile of the vibrational echo. The two excitation pulses are focused and crossed in a sample at an angle θ. The vibrational echo is emitted from the sample at an angle 2θ from that of the first pulse.

are physiologically relevant for biological studies. Further, vibrational echoes probe dynamics on the ground-state potential surface. Therefore, the excitation of the mode causes a minimal perturbation of the solvent. Recently, vibrational echoes have been used to examine vibrational dynamics in liquids, glasses [15, 16] and proteins [17–19].

For experiments on vibrations, a source of picosecond IR pulses is tuned to the transition of interest. The vibrational echo experiment involves a two-pulse excitation sequence. The first pulse excites each solute molecules' vibration into a superposition state, which is a coherent admixture of the $|0\rangle$ and $|1\rangle$ vibrational states. This is depicted in figure 2(*a*). Each vibrational superposition has associated with it a microscopic electric dipole, which oscillates at its vibrational transition frequency. Immediately after the first pulse, all the microscopic dipoles in the sample oscillate in phase. Because there is an inhomogeneous distribution of vibrational transition frequencies, the dipoles oscillate with some distribution of frequencies. Thus, the initial phase relationship is very rapidly lost. This effect is the free induction decay. After a time τ, a second pulse, travelling along a path making an angle θ (figure 2(*b*)) with that of the first pulse, passes through the sample. This second pulse changes the

phase factors of each vibrational superposition state in a manner that initiates a rephasing process. At time 2τ, the ensemble of superposition states is rephased. The phased array of microscopic dipoles behaves as a macroscopic oscillating dipole that generates an additional IR pulse of light. A free induction decay again destroys the phase relationships; so only a short pulse of light is generated. This pulse of light, called the vibrational echo, is emitted by the sample. The vibrational echo pulse propagates along a path that makes an angle 2θ with that of the first pulse. In a NMR experiment, the first pulse and second pulse are $\pi/2$ and π pulses respectively. The pulses are square, and the π pulse is twice the duration of the $\pi/2$ pulse. For a square pulse on resonance, the pulse area is $\mu \cdot \mathbf{E} t/\hbar$, where μ is the transition dipole matrix element and $\mathbf{E}$ is the electric field. In the vibrational echo experiments, the pulses are essentially Gaussian and have the same duration. In the vibrational echo experiment, the pulse area is changed by changing the intensity (electric field) of the pulse rather than the duration. Any two pulse areas will give a vibrational echo signal containing the same information. In practice, the experiments are conducted in the small-flip-angle limit, that is the pulses' areas are much less than $\pi/2$. The signal intensity is proportional to the cube of the laser intensity. In this limit, diagrammatic perturbation theory [20, 21] can be employed to calculate the results of various vibrational echo experiments.

Because the inhomogeneous contributions to the dephasing are identical in the time intervals $0 < t < \tau$ and $\tau < t < 2\tau$ but enter the experiment with opposite sign, they cancel at 2τ. The rephasing at 2τ removes the effects of the inhomogeneous broadening [22]. However, fluctuating forces generated by interaction of the vibrational mode of interest with the dynamic solvent environment produce fluctuations in each oscillation's frequency. Thus, at 2τ the rephasing is imperfect. As τ is increased, the fluctuations produce increasingly large accumulated phase errors among the microscopic dipoles at 2τ, and the signal amplitude of the vibrational echo is reduced. Thus, the vibrational echo decay is related to the fluctuations in the vibrational frequencies, and not the inhomogeneous spread in frequencies. A measurement of the change in vibrational echo intensity with delay between the pulses is an vibrational echo decay curve. An example of a vibrational echo decay curve measured on $Rh(CO)_2acac$ in DBP at 3.4 K and a fit to an exponential are given in figure 3. As can be seen, high-quality data can be obtained in vibrational echo experiments.

The Fourier transform of the vibrational echo decay is the homogeneous line shape [22, 23]. For example, if the vibrational echo decay is an exponential with a decay constant of $T_2/4$, the line shape is a Lorentzian with a full width at half-maximum (FWHM) of $1/\pi T_2$. The vibrational echo makes the vibrational homogeneous line shape (decay of the system's off-diagonal density matrix elements) an experimental observable.

Pure dephasing describes the adiabatic modulation of the vibrational energy levels of a transition caused by fast fluctuations of its environment [24, 25]. Measurement of this quantity provides detailed insight into the fast dynamics of the system. In addition to vibrational pure dephasing time T_2^* and the vibrational lifetime T_1, another contribution to the homogeneous dephasing time is orientational relaxation. Although generally equated with physical rotation of the transition dipole, orientational relaxation is any process that causes the loss of angular correlation of the ensemble of transition dipoles [16, 26]. Both pure dephasing and orientational relaxation are thermally induced processes and will vanish as $T \rightarrow 0$ K. The role of orientational
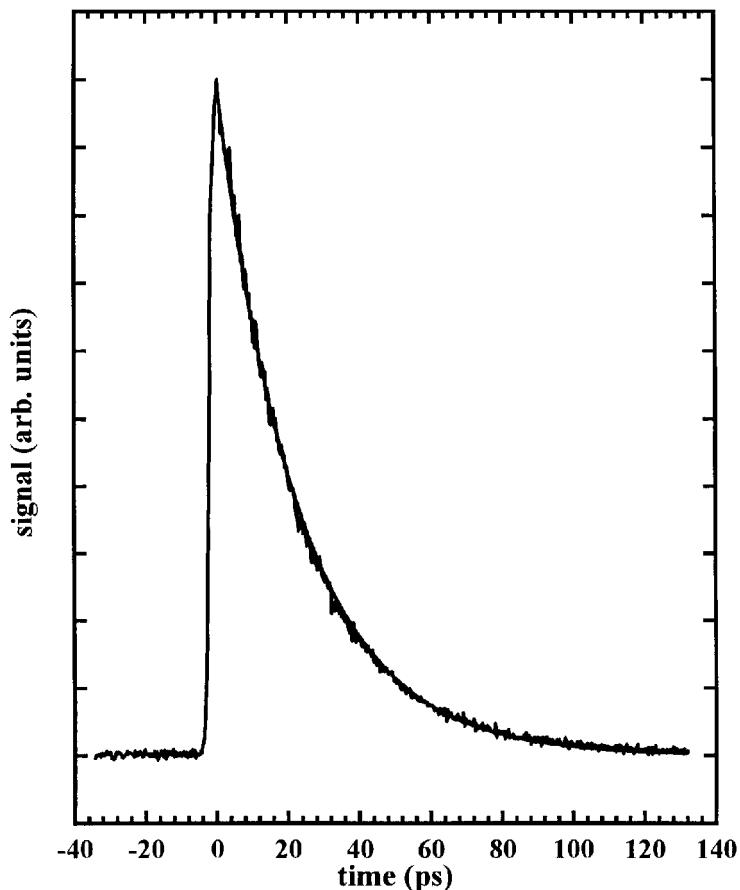
Figure 3.   Vibrational echo decay data for the asymmetric CO stretching mode of $Rh(CO)_2acac$ in DBP at 3.4 K and a fit to a single exponential. The decay is exponential. The decay constant is 23.8 ps, which yields a homogeneous linewidth of 0.11 cm^{-1}. The absorption spectrum has a linewidth of about 15 cm^{-1} at this temperature, demonstrating that the line is massively inhomogeneously broadened.

relaxation in vibrational echo experiments of $W(CO)_6$ has been previously discussed in detail [5] and is discussed briefly below. In the experiments presented below on $Rh(CO)_2acac$ in DBP or on the Mb proteins, orientational relaxation does not occur on the time scale of the vibrational echo experiments because of the samples' high viscosities. This was verified experimentally in all cases using magic-angle pump–probe experiments [17].

The IR absorption line shape is related to these microscopic dynamics through the Fourier transform of the two-time transition dipole correlation function [9–11, 15, 25] which includes any inhomogeneous broadening [3, 9–11, 25]

$$I(\omega) = \mathfrak{F}[C(\tau)] = \frac{1}{2\pi} \int_{-\infty}^{\infty} dt \exp(-i\omega t) \langle \mu(\tau)\mu^*(0) \rangle. \qquad (1)$$

In the Markovian limit and in the absence of inhomogeneous broadening, the two-time transition dipole correlation function decays exponentially at a rate of $1/T_2$,
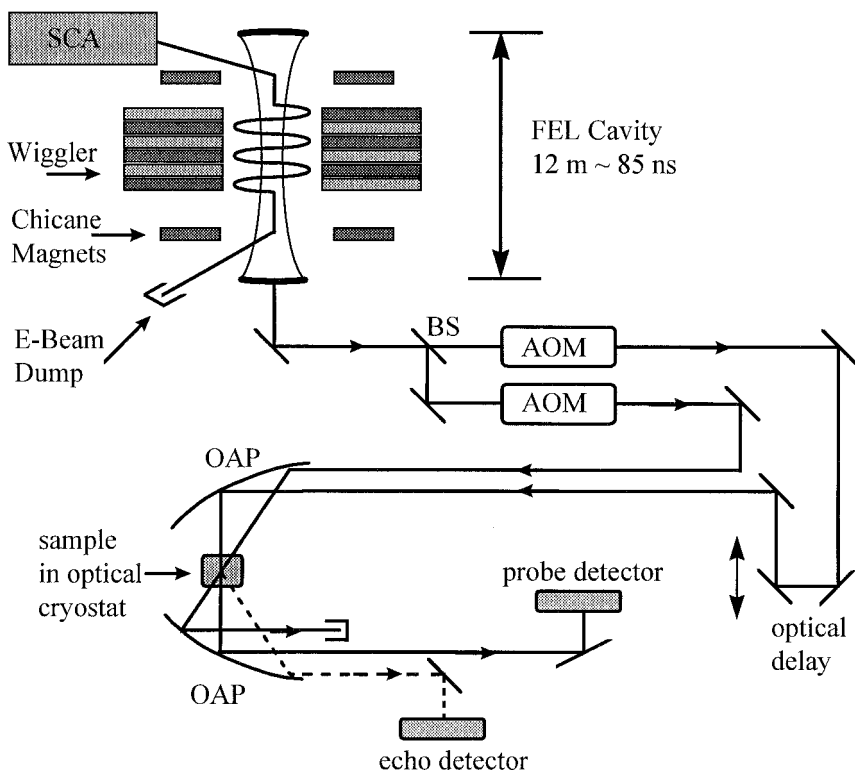
Figure 4. Experimental set-up of vibrational echo and pump–probe experiments at the Stanford Free Electron Laser Center: SCA, superconducting accelerator; BS, beam splitter; AOM, acousto-optic modulator; OAP, off-axis parabolic reflector.

where T_2 is the homogeneous dephasing time. This gives a Lorentzian line shape. Contributions to the full linewidth at half-maximum are additive and, neglecting orientational relaxation, are given by

$$\Gamma = \frac{1}{\pi T_2} = \frac{1}{\pi T_2^*} + \frac{1}{2\pi T_1}. \tag{2}$$

Equation (2) allows the contribution of pure dephasing to the vibrational homogeneous line to be determined from the homogeneous linewidth and the vibrational lifetime.

The vibrational echo, which, as discussed above, eliminates inhomogeneous broadening, is described by a four-time correlation function [14, 27, 28] of the form

$$C(t_1, t_2, t_3) = \langle \mu^*(t_3 + t_2 + t_1)\, \mu(t_2 + t_1)\, \mu(t_1)\, \mu^*(0)\rangle, \tag{3}$$

where t_1, t_2 and t_3 refer to three consecutive time intervals. For a vibrational echo, $t_1 = t_3 = \tau$ and $t_2 = 0$; so the correlation function simplifies to

$$C(\tau) = \langle \mu^*(2\tau)\, \mu(\tau)\, \mu(\tau)\, \mu^*(0)\rangle. \tag{4}$$

(To analyse vibrational echo decays properly when the pulse duration and decay time

are similar, equation (3) is employed [29].) For a vibrational echo signal which decays as an exponential, the correlation function in equation (4) decays as

$$C(\tau) = \exp\left(\frac{-2\tau}{T_2}\right),$$

(5)

where T_2 is the homogeneous dephasing time. The decay of the correlation function describes the decay of the sample's polarization. The signal $I(\tau)$ is related to the square of the absolute value of the polarization, that is

$$I(\tau) = I(0)\exp\left(\frac{-4\tau}{T_2}\right).$$

(6)

(In some circumstances, the vibrational echo decays are much more complex as detailed below [30, 31].)

The correlation function in equations (3) or (4) is normally written as a trace over three nested commutators of the dipole operator with the density matrix using the Heisenberg representation [32]. This form yields eight terms in the total correlation function which contribute to the third-order nonlinear polarization $P^{(3)}$ for a two-level system where the applied field at frequency is resonant (within the laser pulse bandwidth) with the transition frequency. However, only four of these terms will be observed in the vibrational echo phase-matched direction, $k_s = 2k_2 - k_1$. Two of these terms give rise to the vibrational echo (rephasing echo diagrams) and two others contribute to the signal only near $t = 0$ (non-rephasing grating diagrams) [20]. The other four terms only contribute to the vibrational echo signal before $\tau = 0$ and, thus, are not considered further.

The Fourier transform of the four-time dipole correlation function yields the homogeneous line shape:

$$I(\omega) = \mathfrak{F}[|C(\tau)|^2] = \frac{1}{2\pi}\int_{-\infty}^{\infty} dt\,\exp\left(-i\omega t\right)|\langle \mu^*(2\tau)\,\mu(\tau)\,\mu(\tau)\,\mu^*(0)\rangle|^2,$$

(7)

which for an exponential decay of the correlation function gives a Lorentzian line shape

$$I(\omega) = I_0 \frac{T_2}{1 + [2\pi(\omega - \omega_0)]^2\,T_2^2},$$

(8)

where ω_0 is the centre frequency of the vibrational transition. The Lorentzian lineshape will have a FWHM of $1/\pi T_2$ [22].

2.2. *Experimental procedures*

The vibrational echo experiments require tunable IR pulses with durations of about 1 ps and energies of about 1 μJ. The experiments described below were performed using IR pulses of wavelength near 5 μm generated by the Stanford superconducting-accelerator-pumped free-electron laser (FEL). The FEL has been described in detail elsewhere [16, 33, 34]. A schematic diagram of the experimental set-up is given in figure 4. Briefly, an electron bunch is accelerated by the superconducting linear accelerator to relativistic speeds and passed through a wiggler inside an optical cavity. The wiggler is a series of magnets with alternating polarity. The wiggler induces in the electron bunch an oscillatory acceleration transverse to the direction of

propagation. The transverse oscillation causes the emission of radiation at the frequency of the oscillation. Chicanes are used to switch the electron bunches into and out of the cavity, but the optical cavity end mirrors reflect the emitted radiation. The round-trip time of the optical cavity and the time between electron bunches are matched. The result is synchronous pumping of the optical cavity. Changing the energy of the electron beam controls the laser wavelength, and changing the cavity length controls the laser pulse duration. The FEL generates nearly transform-limited pulses with a pulse duration that is adjustable between 0.6 and 2 ps at 5 μm. Active frequency stabilization allows wavelength instabilities to be limited to less than 0.01%, or less than 0.2 cm^{-1} at the 5 μm wavelength of the experiments. The pulse duration, spectrum and peak power are monitored continuously during experiments.

The FEL produces a 2–3 ms macropulse at a 10–20 Hz repetition rate. Each macropulse consists of the picosecond micropulses at a repetition rate of 11.8 MHz (84.7 ns). The micropulse energy at the input to the experimental optics is about 0.5 μJ. In vibrational experiments, virtually all power absorbed by the sample is deposited as heat. To avoid sample heating problems, micropulses are selected out of each macropulse at a repetition rate of 50 kHz by germanium acousto-optic modulator single-pulse selectors [16]. This pulse selection yields an effective experimental repetition rate of 1 kHz, and an average power of less than 0.5 mW.

Both the vibrational echo and the pump–probe experiments utilize a two-pulse excitation sequence. In both cases, a beam splitter is used to split the parent pulse into a weak pulse and an intense pulse. For a vibrational echo, the weak pulse is chopped at about 25 kHz for background subtraction and incident on the sample before the strong pulse. For the pump–probe experiment, the strong pulse is chopped for background subtraction and incident on the sample before the weak pulse. A computer-controlled stepper motor delay line is used to vary the delay between the first and second pulses in both experiments. The two pulses are focused to about 50 μm diameter and crossed in the sample using an off-axis parabolic reflector for achromatic focusing of the IR. The signals are measured using fast IR detectors and gated integrators and are digitized for collection by computer. To switch between measuring the vibrational echo and pump–probe requires changing the detector, the direction of the travel of the delay line, and which of the two pulses is chopped.

Careful studies of power dependence and repetition rate dependence of the data were performed. It was determined that there were no heating or other unwanted effects when vibrational echo experiments were performed with pulse energies of less than 200 nJ and the effective repetition rate of 1 kHz (50 kHz during each macropulse).

2.3. *Sample preparation*

Solutions of Rh(CO)$_2$acac in DBP and W(CO)$_6$ in 2MP, 2MTHF and DBP were made to give a peak optical density (OD) of 0.8 in a 400 μm path length cell. These solutions correspond to mole fractions of 10^{-4} or less. Samples were prepared under a N$_2$ environment. All components used were purchased from Aldrich Chemical Company and used without further purification.

The samples for the temperature studies of native horse heart Mb were prepared by adding 15 mM of lyophilized metMb to 95:5 (w/w) glycerol:0.1 M pH 7 phosphate buffer. The resulting solution was then stirred under a CO atmosphere for 8 h before being reduced by a tenfold molar excess of dithionite. The samples were loaded into a copper cell of 125 μm path length with CaF$_2$ or sapphire windows. The transition had an optical density of about 0.25 on approximately 0.9 background.

The mutant proteins studied were prepared identically with the native Mb in the 95:5 (w/w) glycerol:water sample above. The proteins were synthesized using site-directed mutagenesis techniques [35, 36].

3. Vibrational echo studies of dynamics in liquids and glasses

In this section, a detailed vibrational echo study of $Rh(CO)_2acac$ in DBP above and below the solvent's glass transition temperature ($T_g = 169$ K) is presented and compared with previous results for $W(CO)_6$ in several solvents including DBP [37]. In both metal carbonyls, the asymmetric CO stretching mode at about 2000 cm⁻¹ is examined over a wide range of temperatures. The experiments were performed at temperatures at which the solvent is a low-temperature glass, passes through the glass transition and is a liquid well above T_g. Of particular interest is the pure dephasing time T_2^* which reflects the magnitude of the perturbations of the transition energy which are caused by fluctuations of the bath.

The CO asymmetric stretching modes of $Rh(CO)_2acac$ and $W(CO)_6$ are different in a manner that appears to be important. The $Rh(CO)_2acac$ mode (A_1 symmetry of the molecular point group C_{2v}) is non-degenerate while the $W(CO)_6$ mode (T_{1u} symmetry of the molecular point group O_h) is formally triply degenerate in the gas phase. In a condensed phase, the local solvent structure will be anisotropic. In general, there will be different solute–solvent interactions along the molecular x, y and z axes. These anisotropic interactions will break the triple degeneracy of the T_{1u} mode of $W(CO)_6$, yielding three modes with small energy splittings.

The results presented below show that $Rh(CO)_2acac$ has a temperature-dependent pure dephasing rate with a different functional form than that of $W(CO)_6$ even when the solvent, DBP, is the same. At low temperatures, in glassy DBP, the $Rh(CO)_2acac$ pure dephasing rate is linear in temperature T^1 and is exponentially activated at higher temperature [37]. In contrast, $W(CO)_6$ has a T^2 temperature dependence in three different glassy solvents up to their corresponding T_g values [16]. Above T_g for $W(CO)_6$ in all three solvents, there is a change in the form of the temperature dependence. In 2MP, $W(CO)_6$ pure dephasing makes an abrupt transition from T^2 to a Vogel–Tammann–Fulcher (VTF) type of temperature dependence [16]. Mechanisms are proposed to explain the temperature-dependent pure dephasing of $Rh(CO)_2acac$, and differences between it and $W(CO)_6$, including the role of the different degeneracies of the modes of interest.

3.1. *Liquid–glass results*

Vibrational echo experiments were conducted on the CO asymmetric stretching mode of $Rh(CO)_2acac$ (2010 cm⁻¹) in DBP from 3.4 to 250 K. In addition, vibrational pump–probe experiments were performed on the same transition from 3.4 to 300 K. Figure 3 shows vibrational echo data taken at 2020 cm⁻¹, which is 10 cm⁻¹ to the blue of the centre line, at 3.4 K and a fit to an exponential decay (equation (2)). It was found that the $v = 0$–1 pure dephasing is independent of the laser centre frequency across the vibrational line. However, as discussed below, it is possible to induce multilevel coherences and to observe vibrational echo beats. The laser bandwidth for this data set is about 14 cm⁻¹; so excitation of $v = 1$–2 is negligible. Therefore, the measurement is made on the $v = 0$–1 transition only.

Within experimental uncertainty, the decay shown in figure 3 is a single exponential. Therefore, the homogeneous line shape is a Lorentzian. The T_2 time is 95.2 ps, yielding a homogeneous line width of 0.11 cm⁻¹. For comparison, the absorption spectrum has a line width of about 15 cm⁻¹ at this temperature. The
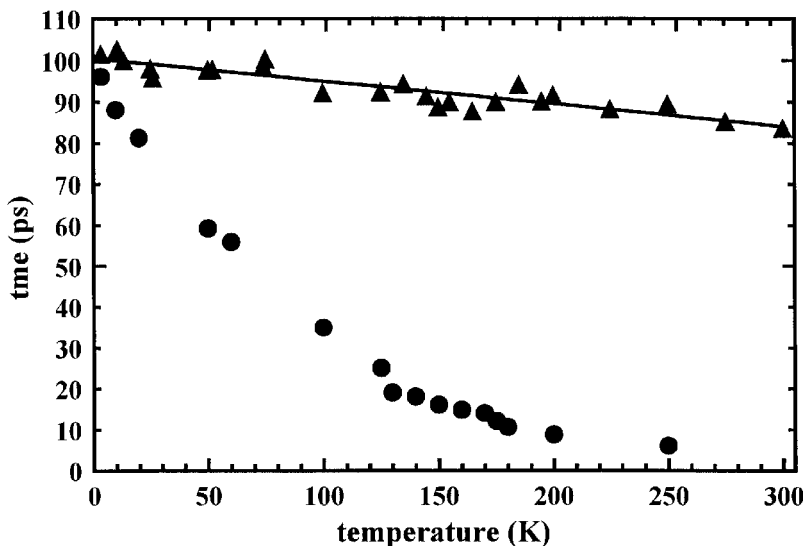
Figure 5. Vibrational echo (●) and pump–probe (▲) data for the asymmetric CO stretch mode of $Rh(CO)_2acac$ in DBP. The pump–probe results are plotted as $2T_1$, for use with equation (2). The solid line through the T_1 data is the best fit to the temperature dependence. Using these results, the temperature-dependent pure dephasing rates can be calculated from equation (2).

absorption line is massively inhomogeneously broadened. The vibrational echo experiments show that the absorption line is inhomogeneously broadened at all temperatures studied, including 250 K ($1/\pi T_2 = 1.5$ cm^{-1}), which is about 80 K above T_g.

Figure 5 displays the results of the temperature dependent vibrational echo (full circles) and pump–probe (full triangles) (plotted as $2T_1$) experiments. As with studies made on $W(CO)_6$ in a number of solvents, the temperature dependence of $2T_1$ is very mild, and the temperature dependence of T_2 is much steeper. Using equation (2) and the $2T_1$ and T_2 values obtained from the experiments, the pure dephasing time T_2^* can be obtained. There is a small amount of scatter in the pump–probe data. The scatter is insignificant at the higher temperatures where pure dephasing totally dominates the homogeneous linewidth. The solid line through the data is a fit to a straight line, which accurately reflects the temperature dependence of the T_1 data over the full range of temperatures. To reduce scatter in the vlaues of T_2^* obtained by removing the contribution from the lifetime, the T_1 values at each temperature were obtained from the linear fit to all of the T_1 data.

Figure 6 displays the values of the pure dephasing time against inverse temperature on semilogarithmic plot [37, 38]. The solid line through the data is a fit to the form

$$\frac{1}{T_2^*} = a_1 T^\alpha + a_2 \exp\left(\frac{-\Delta E}{kT}\right), \tag{9}$$

with $\alpha = 1$ and $\Delta E = 385$ cm^{-1}. The inset is an expanded view of the high-temperature data to show that the data are exponentially activated and that there is no break in the temperature dependence at $T_g = 169$ K. Also shown are dotted and broken curves, for which the α values in equation (9) are fixed at 0.7 and 1.3 respectively, and the other parameters are allowed to float. Within experimental error, $\alpha = 1.0$ gives the best fit to
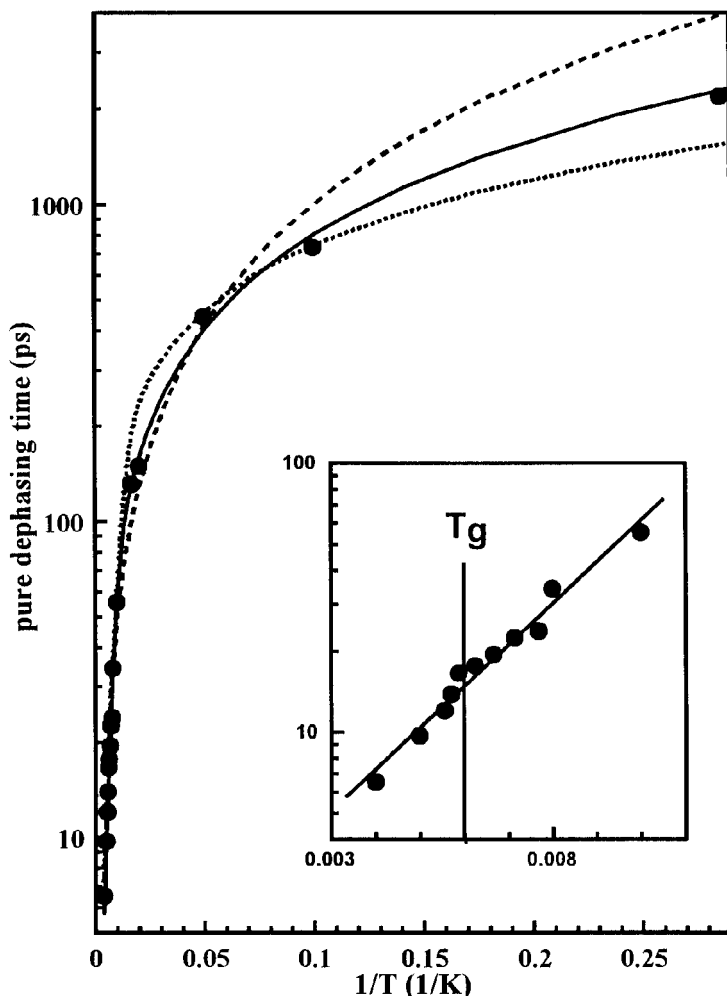
Figure 6. Pure dephasing time of the asymmetric CO stretching mode of $Rh(CO)_2acac$ in DBP against inverse temperature on a semilogarithmic plot. The solid curve through the data is a fit to equation (9), the sum of a power law and an exponentially activated process. The inset is an expanded view at high temperatures showing that the process is activated. Note that there is no break at the experimental T_g, 169 K. The best fit has the power-law exponent $\alpha = 1.0$ and $\Delta E = 385$ cm^{-1}. The dotted and broken curves are for α in equation (9) fixed at 0.7 and 1.3 respectively, and the other parameters of equation (9) allowed to float.

the data, and the value of α has only a very minor effect on the activation energy. By considering a variety of fits such as those displayed in figure 6, the best values for α and ΔE are $\alpha = 1.0 \pm 0.1$ and $\Delta E = 385 \pm 50$ cm^{-1}.

This temperature dependence is fundamentally different from that previously observed for the pure dephasing of the T_{1u} mode of $W(CO)_6$ in three glass-forming solvents. Figure 7(a) shows a reduced variable plot of the pure dephasing of the T_{1u} mode of $W(CO)_6$ in three glassy solvents DBP, 2MP and 2MTHF [16]. The solid curve through the data has a T^2 dependence. Within experimental error, the pure dephasing has a T^2 temperature dependence for all three solvents in spite of the fact that the three
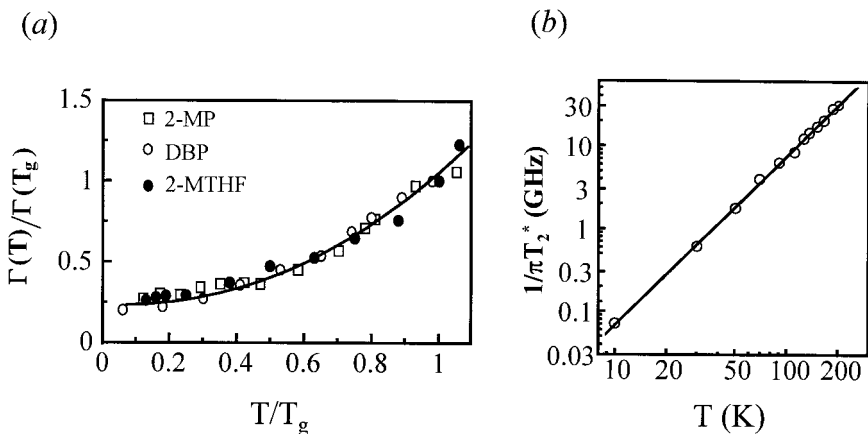
Figure 7.   (a) Reduced variable plot of the homogeneous linewidth of $W(CO)_6$ in DBP, 2MP and 2MTHF. The abscissa is the homogeneous linewidth divided by the homogeneous linewidth at T_g. The ordinate is T scaled by T_g. All data sets fall on the T^2 line. (b) Homogeneous linewidth of $W(CO)_6$ in DBP as a function of temperature with the T_1 contribution removed on a logarithmic plot. The slope of the straight line yields a T^2 dependence.

solvents are quite different. Figure 7(b) shows a logarithmic plot of the homogeneous dephasing data of $W(CO)_6$ in DBP with the contribution from T_1 removed. The solid line through the data has a T^2 dependence. Clearly, the temperature dependence of the pure dephasing of the $W(CO)_6$ and $Rh(CO)_2acac$ in the glassy state is fundamentally different even though the pure dephasing of both molecules is for a CO asymmetric stretching mode at about 2000 cm^{-1} in the same solvent, DBP.

A full temperature dependence of the pure dephasing of the CO mode of $W(CO)_6$ is only available in the solvent 2MP [15, 16]. While $Rh(CO)_2acac$ in DBP does not display orientational relaxation over the range of temperatures studied, $W(CO)_6$ in 2MP does. Orientational relaxation can involve physical rotation of the molecule but can also depend on the degeneracy of the T_{1u} mode [37]. The temperature dependence of the orientational relaxation, as well as T_2 and T_1 have been measured for the T_{1u} mode of $W(CO)_6$ in 2MP [15,16]. Using these, the temperature dependence of the pure dephasing was obtained and is displayed in figure 8 on a logarithmic plot together with the total T_2, $2T_1$ and orientational contribution. At the lowest temperatures, T_2 is dominated by T_1. By about 60 K, the pure dephasing contribution is approximately equal to the lifetime contribution. At higher temperatures, T_2^* dominates the homogeneous line width. The orientational contribution never dominates the linewidth.

Below T_g, the temperature dependence of T_2^* is T^2, as discussed above. Above T_g, there is a dramatic break in the temperature dependence. The solid line through the data is a fit to a VTF equation

$$\frac{1}{\pi T_2^*} = a_1 T^\alpha + a_2 \exp\left(\frac{-B}{T-T_0}\right).$$

(10)

The first term is the T^2 temperature dependence observed in the low-temperature glass; α is 2.0 ± 0.1. The second term has the form of the VTF equation which is often used to describe the onset of dynamic processes above the T_g [39–41]. The VTF
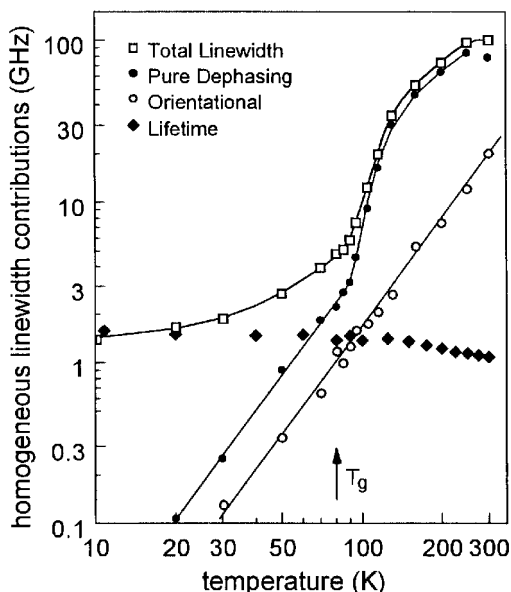
Figure 8. Contributions to the homogeneous linewidth for the asymmetric CO stretch of $W(CO)_6$ in 2MP. The open squares are the temperature-dependent homogeneous linewidth, as determined from the vibrational echo, equation (6). The temperature dependence of each of the contributions is shown. The lifetime contribution (♦) was measured using pump–probe experiments and is the dominant contribution at low temperatures. The pure dephasing contribution was obtained using equation 2 (and also removing the orientational relaxation contribution [30, 31]) and is dominant at high temperatures. The orientational relaxation was determined from magic-angle pump–probe experiments and only makes a significant contribution at intermediate temperatures. The line through the pure dephasing data is a fit to equation (10).

equation describes a process with a temperature-dependent activation energy that diverges at a temperature T_0 below the nominal T_g. T_0 can be linked to an 'ideal' T_g [40]. The temperature dependence of the viscosity of 2MP also has a VTF dependence and gives $T_0 = 59$ K [16]. The fit of equation (10) to the pure dephasing data describes the entire temperature dependence exceedingly well up to 250 K but yields a reference temperature of $T_0 = 80$ K. This reference temperature matches the laboratory T_g, and not ideal T_g. The onset of the dynamics that cause the rapid increase in homogeneous dephasing of $W(CO)_6$ in 2MP is apparently linked with the onset of structural processes near the laboratory T_g.

3.2. *Liquid–glass dephasing mechanisms*
3.2.1. *Low-temperature pure dephasing of* (*acetylacetonato*)*dicarbonylrhodium*(*I*)

Pure dephasing of the form T^α where $\alpha \approx 1$ has been observed for homogeneous pure dephasing of electronic transitions of molecules in low-temperature glasses using photon echoes [3, 12, 13] and hole-burning spectroscopy [1, 42–44]. The electronic dephasing has been described using the two-level system model of low-temperature glass dynamics [3, 42, 45, 46]. The two-level system theory was originally developed in the early 1970s to explain the anomalous heat capacity of low-temperature glasses, which is approximately linear in T [47, 48]. Even at low temperatures, glasses are continuously undergoing structural changes. The complex potential surface on which local structural dynamics occur is modelled as a collection of double wells. At low
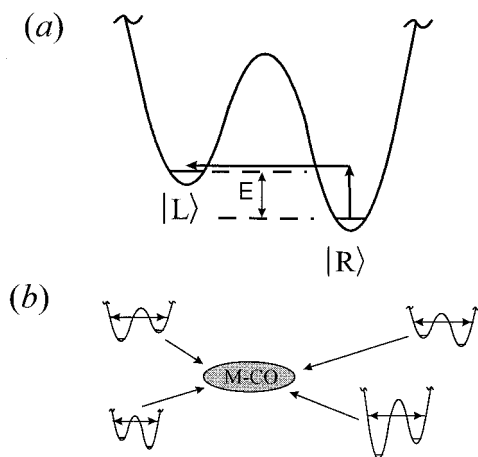
Figure 9.   (*a*) An illustration of a two-level system making a transition from a lower-energy
     local structure in the glass to a higher-energy structure. A glass is modelled as having
     many two-level systems with a broad distribution of tunnelling splittings *E*. (*b*) A
     schematic diagram of the CO oscillator coupled to a number of two-level systems. The
     two-level system transitions produce fluctuating forces at the oscillator, causing pure
     dephasing.

temperatures, only the lowest energy levels are involved; so these are referred to as
two-level systems. Figure 9(*a*) is an illustration of a two-level system. $|L\rangle$ represents
a particular local structure of the glass. $|R\rangle$ represents a different local structure.
Transitions can be made between $|L\rangle$ and $|R\rangle$ by phonon-assisted tunnelling. At very
low temperatures, where the Debye T^3 contribution to the heat capacity is small, the
heat capacity is dominated by the uptake of energy in going from a lower-energy
structure to a higher-energy structure, for example the transition $|R\rangle \rightarrow |L\rangle$ in figure
9(*a*). A glass is modelled as having many two-level systems with a broad distribution
of tunnel splittings *E*. If the probability $P(E)$ of having a splitting *E* is constant, that
is $P(E) = C$ (all *E* are equally probable), then the heat capacity varies as *T*.

   The description of electronic dephasing in low-temperature glasses is based on the
two-level system dynamics [3, 42, 45, 46]. We propose that identical considerations can
apply to the vibrational dephasing of Rh(CO)$_2$acac in DBP at low temperatures.
Figure 9(*b*) illustrates the mechanism. A particular molecule is coupled to a number
of two-level systems. For those two-level systems with *E* not too large ($E \lesssim 2kT$), the
two-level systems are constantly making transition between $|L\rangle$ and $|R\rangle$ with a rate
determined by *E* and the tunnelling parameter [2]. The structural changes between $|L\rangle$
and $|R\rangle$ produce fluctuating strains, referred to as strain–dipole coupling. The
fluctuating strains result in fluctuating forces on the CO oscillator. Thus, the
vibrational pure dephasing can be caused by two-level system dynamics. It has been
demonstrated theoretically using the uncorrelated sudden jump model that, for
$P(E) = CE^\mu$, the temperature dependence of the pure dephasing is $T^{1+\mu}$ [49].
Therefore, for the flat distribution, $\mu = 0$, the pure dephasing temperature dependence
is *T*. *T* and somewhat steeper temperature dependences, for example $T^{1\cdot3}$, have been
observed in electronic dephasing experiments in low-temperature glasses [1, 12, 49].
Recent theoretical work, which has examined the problem in more detail, suggests that
even the apparent superlinear temperature dependences may arise from an energy
distribution $P(E) = C$ [50]. Other theoretical work has investigated the influence of

coupled two-level systems [51]. Regardless of the theoretical approach, the qualitative results are the same. Coupling of a transition to a distribution of tunnelling two-level systems can produce pure dephasing which is essentially dependent on T.

It needs to be stressed that other physical processes can yield similar temperature dependences. For example, a power-law temperature dependence can arise from activation over barriers rather than tunnelling if there is the appropriate broad distribution of activation energies. However, the success of the two-level system model in describing a large variety of distinct experiments adds weight to the current hypothesis.

3.2.2. *High-temperature pure dephasing of* (*acetylacetonato*)*dicarbonylrhodium*(*I*)

Above about 20 K, the T-dependent vibrational pure dephasing is dominated by the exponentially activated process. Electronic dephasing experiments have also shown power-law temperature dependences that go over to activated processes at higher temperatures [52]. However, in the electronic experiments, power-law behaviour is observed only to a few kelvins because typical activation energies for electronic dephasing are 15–30 cm^{-1}. Therefore, the activated process begins to dominate the power-law pure dephasing at lower temperatures than is observed for the CO vibrational pure dephasing of $Rh(CO)_2acac$. The low activation energy for electronic dephasing in glasses has been shown to arise from coupling of the electronic transition to low-frequency modes of the glass [53, 54]. In the vibrational pure dephasing experiments, $\Delta E \approx 400$ cm^{-1}. Thus, the power-law component of the temperature dependence is not masked until higher temperatures.

In the $Rh(CO)_2acac$ in DBP system, the temperature dependence of the pure dephasing changes rapidly above about 20 K. By 100 K, the temperature dependence is well described by the activated process alone (see inset in figure 6). There is no break in the pure dephasing data as the sample passes through T_g. The activation energy $\Delta E \approx 400$ cm^{-1}, is well above the typical cut-off for phonon modes of organic solids [55]. Furthermore, the far-IR absorption spectra of neat DBP show no significant transitions in the region around 400 cm^{-1}, indicating that there is no specific mode of the solvent that might couple strongly to the CO mode. These facts suggest that the high-temperature Arrhenius pure dephasing process is not caused by a motion associated with the glass–liquid solvent, but rather that the pure dephasing arises from coupling of the CO mode to another internal mode of $Rh(CO)_2acac$.

The proposed mechanism is illustrated in figure 10 (*a*). Thermal excitation of a low-frequency mode causes the CO stretching mode transition frequency to shift a small amount $\Delta\omega$. The lifetime of the low-frequency mode is $\tau = 1/R$. During the time period in which the low-frequency mode is excited, the CO superposition state processes at a higher frequency. Thus, a phase error develops. For a small $\Delta\omega$ and a short τ, the phase error is of the order of $\tau\Delta\omega < 1$. This is the slow or intermediate exchange limit [56, 57]. Repeated excitation and relaxation of the low-frequency mode will produce homogeneous dephasing [56, 57].

Over a temperature range in which the energy ΔE of the low-frequency transition is large compared with kT, the rate of excitation of the low-frequency mode increases exponentially with increasing temperature, that is the rate of excitation is $R\exp(-\Delta E/kT)$. Over this same temperature range, the downward rate will be temperature independent or have a weak temperature dependence. From the fit, $\Delta E \approx 400$ cm^{-1} and the highest temperature corresponds to about 170 cm^{-1}; so this condition is met. This system is in the weak-coupling limit, that is the change $\Delta\omega$ in the
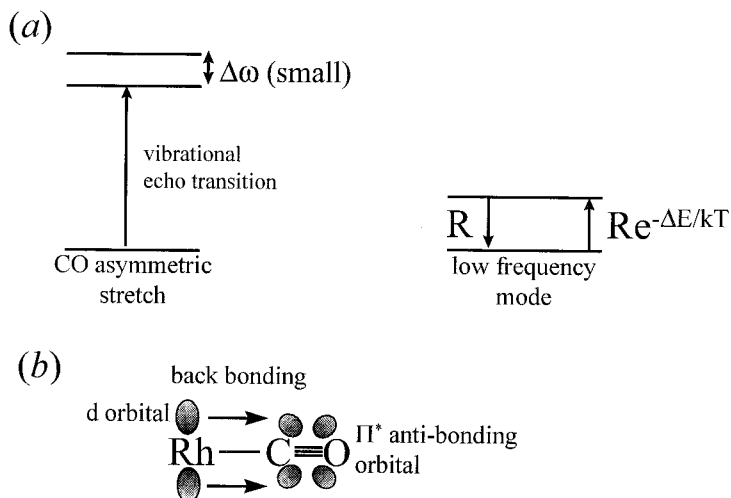
Figure 10. (a) Proposed dephasing mechanism of the asymmetric CO stretching mode of $Rh(CO)_2acac$ at high temperatures. Thermal activation of a low-frequency mode causes a small change $\Delta\omega$, in the transition frequency of the high-frequency mode. During the time when the low-frequency mode is excited, the high-frequency mode develops a phase error. (b) Electron donation from the d_π orbital of the Rh atom to a CO π^* antibonding orbital of CO. Thermal excitation of the Rh–C stretch will lengthen the bond which decreases the magnitude of back bonding, producing a shift to higher energy of the CO transition.

CO frequency with excitation of the low-frequency mode is small compared with the CO frequency. In addition, $\hbar|\Delta\omega|/kT \ll 1$. For these conditions, the pure dephasing contribution to the linewidth from repeated excitation and relaxation of the low-frequency mode is [56]

$$\frac{1}{\pi T_2^*} = \frac{1}{\tau} \frac{(\Delta\omega\,\tau)^2}{1 + (\Delta\omega\,\tau)^2} \exp\left(\frac{-\Delta E}{kT}\right). \tag{11}$$

Equation (11) shows that the contribution to the homogeneous linewidth from the excitation of the low-frequency mode will be exponentially activated. The right-hand side of equation (11) is consistent with equation (9), which was used to fit the data. The factor multiplying the exponential is the constant a_2 in equation (9). This term dominates the temperature dependence at high temperatures.

For the proposed mechanism to account for the observed high-temperature pure dephasing, a mode of about 400 cm^{-1} must couple non-negligibly to the asymmetric CO stretch so that $\Delta\omega$ is significant. The Rh–C asymmetric stretching mode has an transition energy of 405 cm^{-1} [58]. The closest other modes of $Rh(CO)_2acac$ are outside the error bars on the activation energy [58]. There is a reasonable explanation why the Rh–C stretch couples significantly to the CO mode, but modes of lower frequency, which would become populated at lower temperature, do not. The explanation is illustrated in figure 10(b). $Rh(CO)_2acac$ has significant back donation of electron density from the Rh d_π to the CO $p_{\pi*}$ antibonding orbital (back bonding) that weakens the CO bond and red shifts the transition energy about 100 cm^{-1} to approximately 2045 cm^{-1}. (The splitting of the symmetric and asymmetric linear combination of the two CO stretches further shifts the aymmetric mode to the observed value of 2010 cm^{-1}.) Thus, back bonding plays a significant role in

determining the transition frequency. It is well known that in metal carbonyl compounds, the CO frequency is very sensitive to changes in back bonding [59]. Also, a combination of isotope substitution spectroscopic experiments and calculations show that for metal carbonyls, there is substantial coupling between the M–C stretch and the C–O stretch [60]. When the Rh–C mode is thermally excited from the $v = 0$ state to the $v = 1$ state, the average bond length will increase. The increase in the sigma bond length will decrease the Rh d_π–CO $p_{\pi*}$ orbital overlap and, therefore, decrease the magnitude of the back bonding. Thus, excitation of the Rh–C mode causes a blue shift of the CO stretching frequency by decreasing the back bonding [38].

Although data are not available for $Rh(CO)_2acac$, IR absorption measurements on transition metal hexacarbonyls support this mechanism [60]. For the equivalent mode of $M(CO)_6$ (M = Mo or Cr), the combination absorption band of the M–C asymmetric stretch and the CO asymmetric stretch is about 20 cm^{-1} higher in energy than the sum of the two fundamental energies [60]. Thus, the $v = 0 \to 1$ transition of the CO stretch is 20 cm^{-1} higher in energy when the M–C mode is excited ($\Delta\omega \approx 20$ cm^{-1}). The change in back bonding upon excitation of the Rh–C mode provides a direct mechanism for coupling excitation of the Rh–C stretch to the CO stretch transition frequency. Other low-frequency modes, such as a methyl rocking mode of the acac ligand, will not have this direct coupling and, therefore, will not cause pure dephasing even though they may be thermally populated.

If the proposed mechanism is valid, it should be possible to estimate τ using a_2 in equation (9) and $\Delta\omega$:

$$a_2 = \frac{1}{\pi\tau} \frac{(\Delta\omega\,\tau)^2}{1 + (\Delta\omega\,\tau)^2}. \tag{12}$$

The value of a_2 is obtained from the data in figure 6: $a_2 = 1.2$ THz. As discussed above, based on compounds similar to $Rh(CO)_2acac$, $\Delta\omega \approx 20$ cm^{-1}. Using the values for a_2 and $\Delta\omega$ yields a value for τ of 0.75 ps. This should be the vibrational lifetime of the 405 cm^{-1} Rh–C stretch. To our knowledge, a direct measurement of the lifetime of this mode or of any low-frequency vibration has not been made. However, 0.75 ps is a reasonable number. It is plausible that Rh–C relaxes via a cubic anharmonic process involving the annihilation of the original Rh–C excitation and the creation of two lower-frequency modes [58] $Rh(CO)_2acac$ has several internal lower-frequency modes [58]. One possible relaxation pathway is to create one internal mode, for example 300 cm^{-1}, and to create a mode of the solvent continuum, assuring conservation of energy. Another possible pathway is relaxation into two modes of the solvent continuum. For a non-hydrogen bonding solvent such as DBP, the continuum of translational and orientational modes (instantaneous normal modes [61, 62]) will extend to several hundred reciprocal centimetres [63]. For either possibility, the low-order cubic anharmonic processes available for the relaxation and the high density of states provided by the solvent continuum will cause rapid relaxation of the Rh–C vibration. In the future, it should be possible to perform a far-IR pump–probe experiment to make a direct measurement of the Rh–C lifetime.

3.2.3. *Dephasing of* $W(CO)_6$

As can be seen from a comparison of figures 6–8, the temperature-dependent pure dephasing of $Rh(CO)_2acac$ is fundamentally different from that of $W(CO)_6$ at all temperatures even though an asymmetric CO stretch at about 2000 cm^{-1} was studied in both molecules. It is proposed that the $W(CO)_6$ pure dephasing is different because
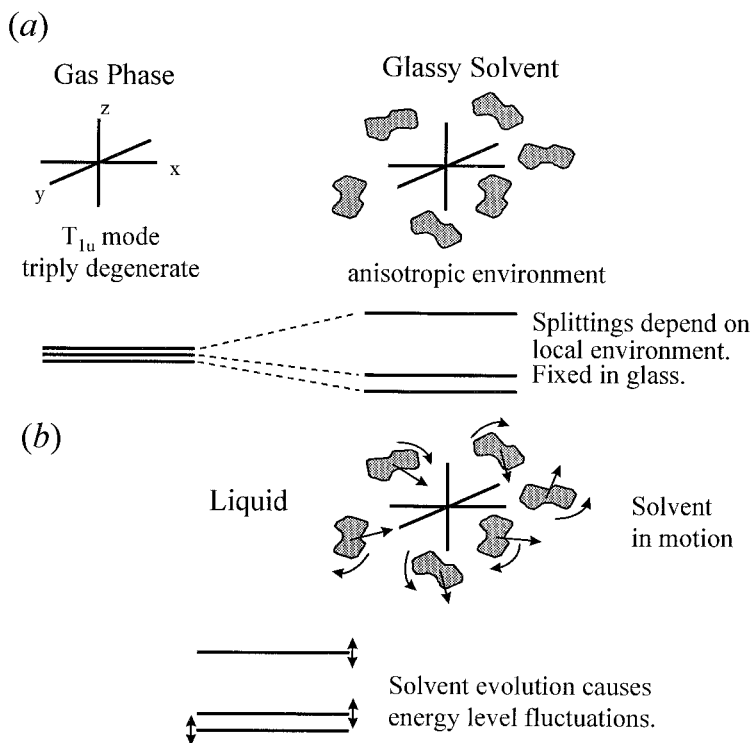
Figure 11. (a) In the gas phase, the T_{1u} mode of $W(CO)_6$ is triply degenerate. In a condensed phase, such as a liquid or glass, the anisotropic environment breaks the degeneracy, producing three levels with small energy splittings. (b) Solvent molecular motions in the liquid state produce a local time-dependent anisotropic structure. Fluctuations in local structure couple to the three levels, causing energy level fluctuations and pure dephasing.

of the high symmetry of the T_{1u} asymmetric CO stretching mode, which is triply degenerate in the gas phase [60], while the $Rh(CO)_2acac$ mode is not degenerate. The $W(CO)_6$ T_{1u} mode consists of all six CO moving in concert, one pair along the molecular x axis, one pair along y and one pair along z. In a liquid or glass, the solvent structure is locally anisotropic. In general, there will be different solute–solvent interactions (forces exerted on the oscillator) along x, y and z. These interactions will break the triple degeneracy, yielding three modes with some energy splittings. This model is illustrated in figure 11 (a). There will be a range of such splittings reflecting the range of local solvent structures.

In a glass, the local solvent structure about a $W(CO)_6$ molecule is essentially fixed on the time scale of the pure dephasing. The T^2 temperature dependence in the three glassy solvents studied suggests a two-phonon process in the high-temperature limit, that is $kT > \hbar\omega_p$, where ω_p is a typical phonon frequency involved in the two phonon process. Two-phonon elastic scattering that causes fluctuations in the anisotropic local solvent structure surrounding $W(CO)_6$ will induce fluctuations of the level splittings and can cause pure dephasing.

A second mechanism that would result in a T^2 temperature dependence is two-phonon scattering from one level to another. This mechanism is referred to as inelastic two-phonon scattering. This second possibility can be ruled out. The non-degenerate levels will be approximately along the molecular x, y and z axes. The modes will be

approximately the basis modes of the triply degenerate state, although there will be some mixing caused by the anisotropic nature of the solvent perturbation. Scattering among the levels would result in orientational relaxation since it would take the oscillating dipole from, for example, x to y or z. If two-phonon inelastic scattering among the three non-degenerate levels was responsible for the pure dephasing, it would occur at the same rate as the orientational relaxation. In the glass and liquid states of the solvent, the contribution of orientational relaxation to the total homogeneous line width has been analysed (see figure 8), and it is small compared with pure dephasing [5].

In the previous studies, orientational relaxation, which was shown not to depend on physical rotation of the molecule, was ascribed to the triply degenerate nature of the T_{1u} state [15, 16]. It was implicitly assumed that the state was actually degenerate, and that the radiation field would excite some particular coherent superposition of the x, y and z basis states. However, because the degeneracy will be broken by the anisotropic environment, a single state will be excited. The probability of exciting x, y or z will depend on the projection of the excitation E field onto the x, y and z axes. Then, the overall proposal is that orientational relaxation is caused by two-phonon inelastic scattering among the three non-degenerate states and, in the glass, pure dephasing is caused by two-phonon elastic-scattering-induced energy fluctuations of the x, y and z levels. Because the T_{1u} mode is degenerate, any anisotropic perturbation will break the degeneracy. The resulting splittings should be very sensitive to even small phonon-induced fluctuations of the local solvent environment. This is not a mechanism that is available to $Rh(CO)_2acac$. Apparently the two-phonon elastic scattering mechanism available to $W(CO)_6$ dominates the mechanisms responsible for pure dephasing of $Rh(CO)_2acac$ in the glass and liquid states.

The temperature dependence of the total homogeneous linewidths of $W(CO)_6$ changes abruptly above T_g in the three solvents DBP, 2MTHF and 2MP [15, 16]. In DBP and 2MTHF, there is evidence of motional narrowing [15, 16]. The pure vibrational dephasing above T_g in 2MP has a very steep VTF temperature dependence (see figure 8). In the liquid, the solvent structure surrounding $W(CO)_6$ is no longer static on the homogeneous dephasing time scale. Translational and rotational motions of the solvent will produce fluctuating forces that do not occur below T_g (see figure 11(b)). Thus, there is a change from a two-phonon elastic scattering mechanism, with essentially fixed solvent structure below T_g, to a mechanism that involves the evolution of the local anisotropic solvent structure above T_g.

The evolution of the local solvent structure will cause the splittings of the three closely spaced levels to evolve in time, inducing pure dephasing. Thus, the triply degenerate nature of the $W(CO)_6$ T_{1u} mode is also intimately involved in the pure dephasing in the liquid, but the nature of the solvent dynamics changes above T_g, causing an abrupt change in the temperature dependence. In the proposed mechanism, the pure dephasing of $W(CO)_6$ in liquid 2MP is caused by the very-high-frequency solvent motions that are ultimately responsible for longer-time-scale processes such as translational and rotational diffusion and dielectric relaxation. The observed VTF temperature dependence would seem to be consistent with this dephasing mechanism.

4. Vibrational echo beat spectroscopy

Vibrational echo data can have two forms which are dependent on the vibrational anharmonicity, the laser bandwidth and the laser frequency. In the case where the vibrational anharmonicity is large compared with the laser bandwidth or the laser

frequency is properly tuned, only the $v = 0$–1 transition is excited. The vibrational echo decays are exponential [16] as discussed above and shown in figure 3. However, if shorter pulses are used in the vibrational echo experiments, it is possible for the pulse bandwidth to exceed the anharmonic splitting. In this case, a three level coherence involving the $v = 0$, 1 and 2 levels is formed. This produces a non-exponential vibrational echo decay with beats at the anharmonic splitting frequency as shown in figure 12 [30, 31]. The VEB experiment yields the vibrational anharmonic splitting as well as the vibrational pure dephasing of both the $v = 0$–1 and 1–2 transitions. Measurements of vibrational anharmonicities provide information about the shape of the vibrational potential surface. They can be obtained using conventional absorption spectroscopy, but this method is difficult because very weak overtone spectra must be measured. Two colour IR time-resolved pump–probe experiments have been used to measure vibrational anharmonicities [64, 65]. These experiments require two pico-second IR pulses with different characteristics, that is wavelength and bandwidth.

The VEB experiment does not produce a conventional quantum beat. In a quantum beat, a state is coupled by the radiation field directly to two other states that fall within the bandwidth of the pulse. In the VEB experiment, the radiation field couples $v = 0 \rightarrow 1$ and then $v = 1 \rightarrow 2$. There is no direct coupling between $v = 0 \rightarrow 2$. At the polarization level, for Lorentzian homogeneous lines the vibrational echo decay is a biexponential. One exponential corresponds to the decay of the $v = 1$–2 coherence and the other exponential corresponds to the decay of the $v = 0$–1 coherence. At the intensity level, there is a cross term and a beat. Using the theory outlined below, both coherence decay times can be extracted from the data. Furthermore, with the same laser parameters that give a VEB decay, the pump–probe experiment yields a biexponential decay. The time constants of the decay are the lifetimes of the $v = 2$ and $v = 1$ levels. Therefore, using both T_2 values from the VEB and both T_1 values, it is possible to obtain both T_2^* values for the three-level system.

Previous theoretical work on a three-level vibrational echo described an equally spaced system [66]. The derivation of the VEB signals for three-level systems has a large contribution from experiments and theory studying coherent oscillations in semiconductor structures [67, 68]. The vibrational echo signal can be described for an unequally spaced three-level system using a semiclassical diagrammatic perturbation theory treatment of the third-order nonlinear polarizability [20, 32]. The three-level system is spaced by the frequencies ω_{01} and ω_{12}, where $\omega_{01} = \omega_{12} + \Delta$, and $|\Delta| \ll \omega_{01}$ and ω_{12}. Δ is the anharmonic vibrational energy splitting. The transition frequencies ω_{01} and ω_{12} lie within the bandwidth of the pulses. For such a system, three independent resonant pathways (diagrams) exist that result in rephasing and the generation of the vibrational echo pulse. In addition to the two that describe rephasing in a two-level system (as mentioned above) [20], a third diagram accounts for the possibility of rephasing the $v = 1$–2 coherence. For a finite pulse bandwidth, where the E-field amplitude differs at ω_{01} and ω_{12}, the decay is given approximately by [31]

$$I(\tau) = I(0)\exp\left(\frac{-2\tau}{T_2(01)}\right)\left\{(E_{01}\,\mu_{01})^2\exp\left(\frac{-2\tau}{T_2(01)}\right) + (E_{12}\,\mu_{12})^2\exp\left(\frac{-2\tau}{T_2(12)}\right)\right.$$

$$\left. - 2(E_{01}\,\mu_{01})(E_{12}\,\mu_{12})\exp\left[-\left(\frac{\tau}{T_2(01)} + \frac{\tau}{T_2(12)}\right)\right]\cos(\Delta\tau + \phi)\right\}. \qquad (13)$$

Here, E_{01} and E_{12} are amplitudes of the electric fields at the respective transitions and μ_{01} and μ_{12} are the respective dipole transition matrix elements which are constant.

$T_2(01)$ and $T_2(12)$ are the corresponding homogeneous dephasing decay constants, and Δ is the vibrational anharmonic splitting frequency (the beat frequency in the signal). $I(0)$ contains all the factors that determine the strength of the signal but are not involved in either the time-dependent decays or the wavelength dependence of the beats. The homogeneous dephasing rates $T_2(01)$ and $T_2(12)$ for the two transitions are phenomenological; no model has been assumed for the coupling of these modes to the bath. For the narrow-bandwidth case ($E_{12} = 0$), equation (6) is recovered.

To compare equation (13) with data requires a convolution to account for the finite pulse duration. To extract a vibrational echo decay that is on the same time scale as the pulse duration requires full consideration of the three time-ordered interactions of the radiation fields with the vibrations. In these experiments, the vibrational echo decays are long compared with the pulse durations; so this procedure is unnecessary. However, the beat frequency is comparable with the pulse duration. Therefore, in the data, the beats appear with much less depth of modulation than they would have in the absence of a finite instrument response. To account for this, equation (13) is convolved with the vibrational echo time dependence that would be observed for a sample with delta function response. This is defined as the instrument response function. For finite instrument responses, the data are fitted by

$$ S(\tau) = \mathfrak{F}^{-1}\left(\mathfrak{F}\left\{p\left[\left(\frac{3}{2}\right)^{1/2} t\right]\right\} \mathfrak{F}[I(\tau)]\right), \tag{14} $$

where $\mathfrak{F}$ and $\mathfrak{F}^{-1}$ are Fourier transform and inverse Fourier transform respectively. $I(\tau)$ is from equation (13), and $p(t)$ is the laser pulse envelope at the intensity level. In these experiments, the pulse envelope is essentially a transform-limited Gaussian. The factor $(\frac{3}{2})^{1/2}$ arises from the three interactions of the two Gaussian pulses used in the vibrational echo experiment [30].

Figure 12(a) displays data obtained for $Rh(CO)_2acac$ in DBP at 3.4 K using a frequency of 2004 cm^{-1}. The centre of the $v = 0$–1 transition is at 2010 cm^{-1}. These data are thus taken with the frequency tuned somewhat to the red of the line centre. The pulse bandwidth is 8 cm^{-1} FWHM, which corresponds to a 1.3 ps pulse duration. A fit to the data is also shown. The fit uses equations (13) and (14) with a 1.6 ps FWHM instrument response. Figure 12(b) shows the same data but with a fit to equations (13) and (14) that holds the cosine term constant at unity, that is the decay kinetics are the same but there are no beats in the fitting function. The inset in figure 12(b) are the residuals, which contain only the beats. Δ, the anharmonicity (the difference between the $v = 0$–1 and the $v = 1$–2 transition frequencies) can be obtained from the fit in figure 12(a) or it can be read off directly from the inset in figure 12(b). The results yield $\Delta = 13.5 \pm 0.2$ cm^{-1}.

In the fit to equations (13) and (14), the fast component corresponds to the homogeneous dephasing time $T_2(12)$ of the $v = 1$–2 vibrational coherence and the slow component corresponds to the homogeneous dephasing time $T_2(01)$ of the $v = 0$–1 vibrational coherence. As can be seen from both figure 12(a) and figure 12(b), the fits to the data are quite good. The decay constants yield homogeneous dephasing times of $T_2(12) = 15$ ps and $T_2(01) = 95$ ps. Thus, $T_2(12)$ can be extracted from a VEB experiment [30, 31].

Equation (13) predicts that the magnitudes of the components of decay and the amplitude of the beats are related to the strengths of the E fields at the two transition frequencies. For a finite bandwidth pulse, as the excitation frequency is moved from
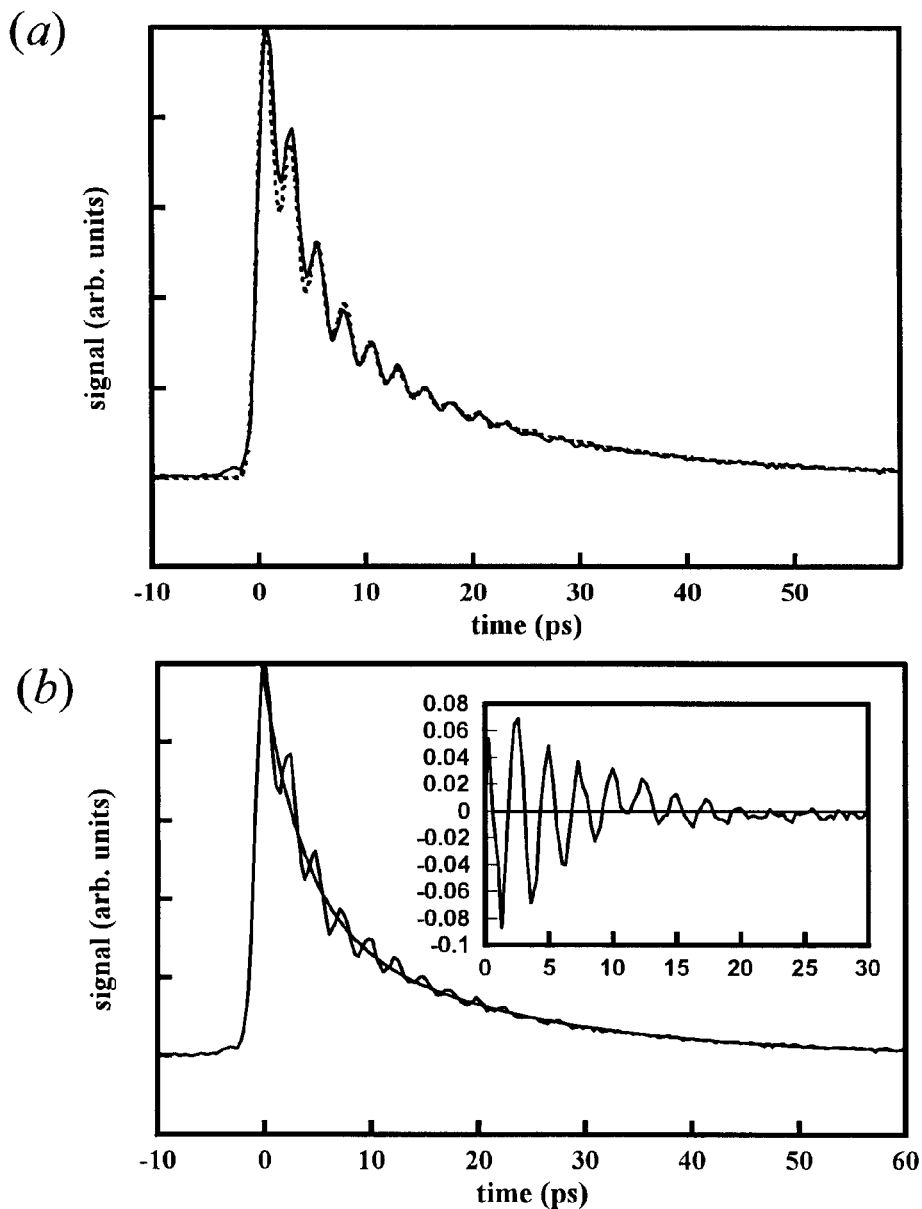
Figure 12.   (*a*) Vibrational echo decay for $Rh(CO)_2acac$ in DBP at 3.4 K and 4.99 μm. Fit shown is using equations (9) and (10) and represent the homogeneous dephasing of the three-level coherence with beating at the anharmonic vibrational frequency splitting. (*b*) Vibrational echo decay for $Rh(CO)_2acac$ in DBP at 3.4 K and 4.99 μm fit to equation (9) with the oscillator term held constant. The inset are the residuals of the fit, which display only the beats.

around the peak of the $v = 0$–1 transition to lower energies, the beats will become more pronounced, and the component of the decay corresponding to the relaxation of the $v = 1$–2 coherence will become larger. Figure 13(*a*) displays $Rh(CO)_2acac$ vibrational echo data taken at 3.4 K at a variety of frequencies. The centre of the $v = 0$–1 transition is 2010 cm^{-1}. The uppermost data set is at 2020 cm^{-1}. In this data
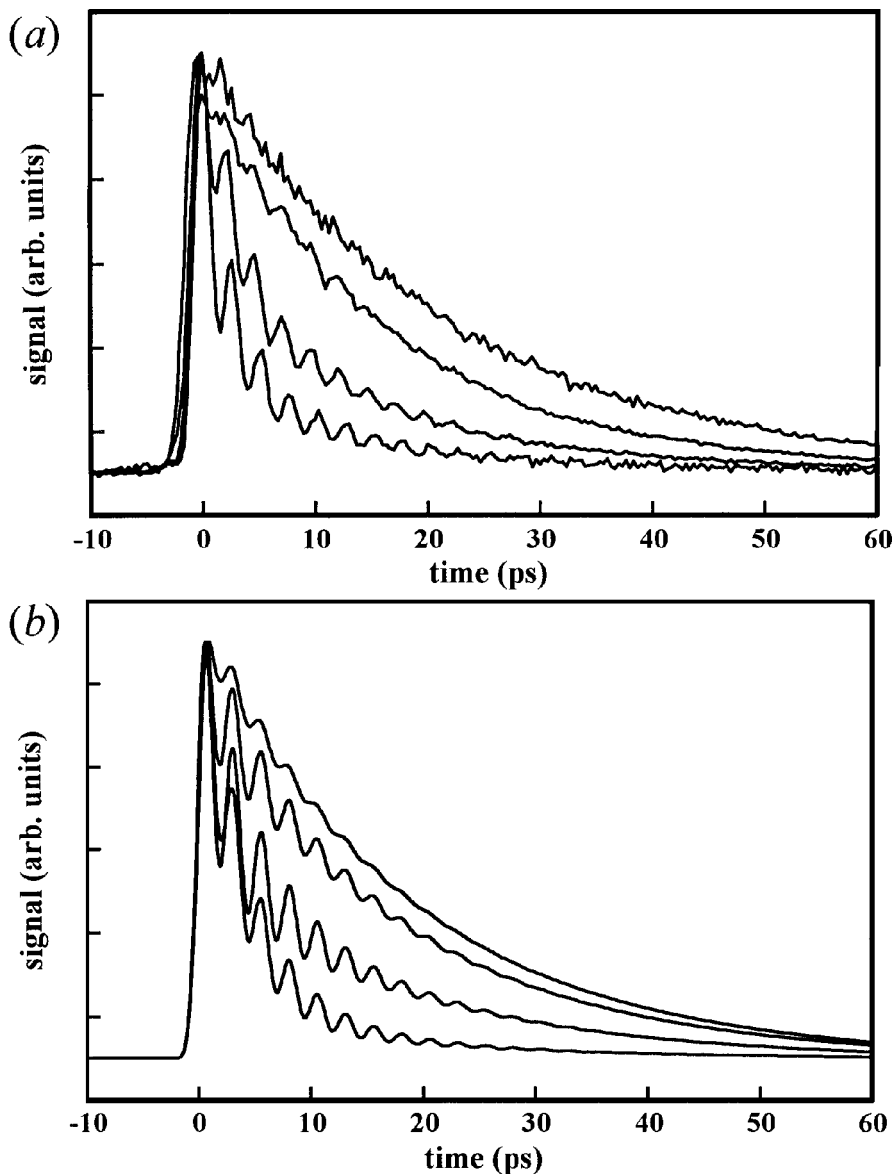
Figure 13. (*a*) Wavelength dependence of VEB experiments of $Rh(CO)_2acac$ in DBP at 3.4 K. The centre transition wavelength is at 2010 cm^{-1}. Frequencies studied, from top to bottom, are at 2020, 2012, 2004 and 1996 cm^{-1}. (*b*) Calculation of an excitation wavelength dependence of a VEB signal using equation (13). The curves were convolved with a 1.6 ps instrument response. The decay constants, beat frequencies and phases used were similar to those obtained in the $Rh(CO)_2acac$ system. Lines, from top to bottom in (*b*), have ratios of the *E* fields at the $v = 0 \rightarrow 1$ and $v = 1 \rightarrow 2$ transitions of 99.5/0.5, 95/5, 67/33 and 20/80 respectively.

set, there are no apparent beats. These data can be fitted with a single exponential (equation (6)). At this laser frequency, there is little or no overlap of the pulse bandwidth with the $v = 1$–2 transition. The single-exponential decay yields $T_2(01)$ only. Tuning to lower energy, 2012 cm^{-1}, there are only very-low-amplitude beats,

which are almost lost in the noise. However, the data cannot be fitted well to a single-exponential decay. To obtain a good fit, equations (13) and (14) are needed. This frequency is still to the blue of the line centre of the $v = 0–1$ transition; so the overlap of the pulse bandwidth with the $v = 1–2$ transition is small. The next data set, at 2004 cm^{-1}, definitely displays beats. In this case, there is significant overlap of the pulse bandwidth with the $v = 1–2$ transition, and the beat amplitude and fast decay component magnitude increase markedly. Finally, the 1996 cm^{-1} data set shows significant beats as there is now extensive overlap of the excitation bandwith with the $v = 1–2$ transition. All data sets indicate that the homogeneous dephasing times of the $v = 1–2$ and $v = 0–1$ transitions are 15 ps and 95 ps respectively.

Figure 13(*b*) shows calculated vibrational echo decays obtained using equations (13) and (14) for several ratios of the *E*-field amplitudes. These curves use dephasing times, beats frequencies and phases determined from the Rh(CO)$_2$acac data and have been convolved with a 1.6 ps FWHM instrument response. From top to bottom, the curves have ratios of the $v = 0–1$ and $v = 1–2$ transition *E* fields of 99.5/0.5, 95/5, 67/33 and 20/80 respectively. In the calculations, $\mu_{12} = 2^{1/2}\mu_{01}$, as is the case for a harmonic oscillator. As the quotient of the two *E* fields decreases, the amplitudes of the beats increase, and there is an increased short time decay of the signal because the contribution of the $T_2(12)$ portion of the signal is increased. The magnitude of the beats in the simulation is also a function of the instrument response compared with the beat frequency. For all the data presented, the instrument responses are in the 1 ps range. Since the beat frequencies are 2–5 ps, depending on the sample, the instrument response significantly decreases the observed magnitude of the beats. The calculations presented in figure 13 (*b*) are qualitatively very similar to the data presented in figure 13 (*a*). This demonstrates the basic validity of the description of the multilevel coherence and its frequency dependence. However, the analytical expression given in equation (13) was derived for a delta function duration pulse, with the standard type of derivation modified to include different *E* fields at the two transition frequencies. A quantitative theoretical description of this problem cannot be obtained analytically because it will include finite pulse durations with finite bandwidths. This produces a complicated numerical problem that is under investigation [69]. As shown above, equation (13) provides a good description of the results. Because it is analytical, it is very useful in data fitting. It gives all parameters correctly except the depth of the beats.

VEB measurements can be made on a large variety of systems. Figure 14 shows data taken on the CO stretching mode of H64V, a Mb mutant, in 95:5 (w/w) glycerol:water at 3.4 K with the laser tuned to 1957 cm^{-1} [30]. The centre of the $v = 0–1$ transition for this line is 1969 cm^{-1}. The excitation bandwidth for the data was about 16 cm^{-1} FWHM. When the vibrational echo decay is measured on the line centre, the data show a single-exponential decay without beats. IR pump–probe experiments measured the $v = 0–1$ lifetime at this temperature as 35 ps [17]. Comparison of the line centre vibrational echo decay and the pump–probe data demonstrate that, at these low temperatures, the homogeneous dephasing time is approximately twice the lifetime, namely $2T_1$, that is there is no significant pure dephasing. From the fit to the data, the homogeneous dephasing times of $T_2(12) = 20$ ps and $T_2(01) = 65$ ps. The fit also gives the beat frequency. The inset in figure 14 displays only the beats, obtained in the same manner as described for figure 12(*b*). From the data, the anharmonicity of 25.4 ± 0.2 cm^{-1} is determined. This can be compared with the approximately 26 cm^{-1} anharmonicity reported for Mb–CO, which
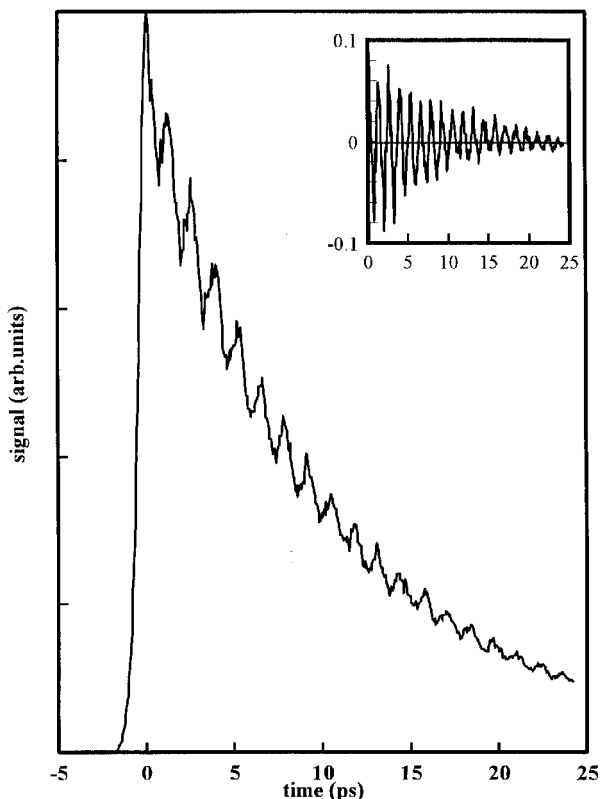
Figure 14.   VEB decay of H64V–CO in glycerol:water at 3.4 K with the laser tuned to 1957 cm^{-1}. The centre of the $v = 0 \rightarrow 1$ transition for this line is 1969 cm^{-1}. The excitation bandwidth was about 16 cm^{-1} FWHM. Like figure 12(*b*), the inset shows the beat data only.

was measured using two colour pump–probe experiments [64, 65]. By using a pulse duration of 670 fs FWHM and tuning to lower frequency than the $v = 0$–1 line centre, it was possible to measure the moderate anharmonicity of H64V. Using available technology, it should be possible to measure even large anharmonicities of 100 cm^{-1} or more.

5.   Vibrational echo studies of protein dynamics

The understanding of protein dynamics is fundamental in understanding the connection between protein structure, as determined by X-ray [70–72], NMR [73] or other experimental techniques [74–78] or theory [79], and protein function. Degenerate four-wave mixing experiments, such as vibrational echoes [17–19], photon echoes [80], hole burning [1] and other ultrafast techniques [65, 75, 81–86] have shown great promise in obtaining crucial information about ultrafast protein motions unobtainable with other methods.

Much of this work has studied Mb, a small 153 amino acid protein which has the primary biological function of the reversible binding and transport of O_2 in muscle tissues. Mb's ability to bind O_2, and other biologically relevant ligands, such as CO or NO, is due to a non-peptide prosthetic group, haem, which is covalently bound at the proximal histidine of the globin. The interior of the protein consists almost entirely of non-polar amino acids while the exterior part of the protein contains both polar and

non-polar residues. The only internal polar amino acids are two histidines [87]. As shown in figure 1 (*b*), the proximal histidine is covalently bonded to the Fe, forming the fifth coordination site of the haem. The sixth coordinate site of the haem is the active site of the protein where the ligand binds. The distal histidine is physically near the sixth coordinate site of the haem but not directly covalently bonded to it. When bound to Mb, the CO vibrational frequency is substantially red shifted from the gas-phase frequency and separated into several distinct bands, labelled A_0, A_1 and A_3 in order of decreasing carbonyl frequency. Although the intensities and widths of these bands are sensitive to temperature, pressures and pH, the peak frequencies remain largely unchanged [88]. These three bands, which occur at 1969 cm^{-1}, 1945 cm^{-1} and 1930 cm^{-1}, reflect distinct protein conformational substates [77].

Molecular dynamics simulations show that Mb has a flexible structure in constant motion at room temperature [79]. Such motions can be either on a relatively small scale involving a few of the constituent atoms, such as the torsion of an amino acid residue, or they can be large-scale motions involving entire regions of the protein backbone. Simulations over a period of 300 ps indicate that Mb samples thousands of local energy minima of approximately equal energies, separated by barriers of varying height [79]. These minima correspond to different conformational substates of the protein. It has been proposed that this characteristic of proteins is analogous to the energy landscape in glasses [89].

5.1. *Vibrational echo results and dephasing mechanisms*

Figure 15 (*a*) displays a vibrational spectrum of the CO bound to Mb. The CO peak is located at 1945 cm^{-1}. Its width is about 15 cm^{-1} at room temperature. As is clear from the spectrum, the CO peak is located on a very large background composed of weak but high-concentrations absorbers of both the protein and the solvent. In spite of the fact that the background absorbs 90% of the incoming excitation pulses and 90% of the outgoing vibrational echo signal, it is still possible to obtain high-quality data. A vibrational echo decay taken on Mb–CO at 60 K is shown in figure 15 (*b*). The high-quality data obtained on Mb–CO and related proteins under less than ideal spectroscopic conditions are important. It demonstrates that the vibrational echo technique is not restricted to samples in which the peak of interest is isolated from all other absorptions. This topic will be addressed further in section 6, where a vibrational echo method for suppressing the background in a spectrum is described.

Figure 16 shows temperature-dependent data on the A_1 band of Mb–CO in 95:5 (v/v) glycerol:water [17]. The squares are twice the $v = 1$ vibrational lifetime of the CO mode, as determined from the IR pump–probe experiment. The lifetime has a slight linear temperature dependence. The full triangles are the measured homogeneous dephasing times T_2 determined by vibrational echo experiments. The homogeneous dephasing has a much steeper temperature dependence than the vibrational lifetime. The full circles are the calculated pure dephasing time T_2^* determined using equation (2). The pure dephasing is the dominant contribution to the homogeneous dephasing at high temperatures and the vibrational lifetime is the dominant component at low temperatures. As mentioned above, a third possible component to the homogeneous dephasing, orientational relaxation, is not observed for Mb–CO in any solvent.

Figure 17 shows the pure dephasing rate $1/\pi T_2^*$ against temperature on a logarithmic plot. The line through the data is a fit to equation (9) with $\alpha = 1.3 \pm 0.1$ and $\Delta E = 1000 \pm 250$ cm^{-1} [17]. The CO pure dephasing is caused by fluctuations of
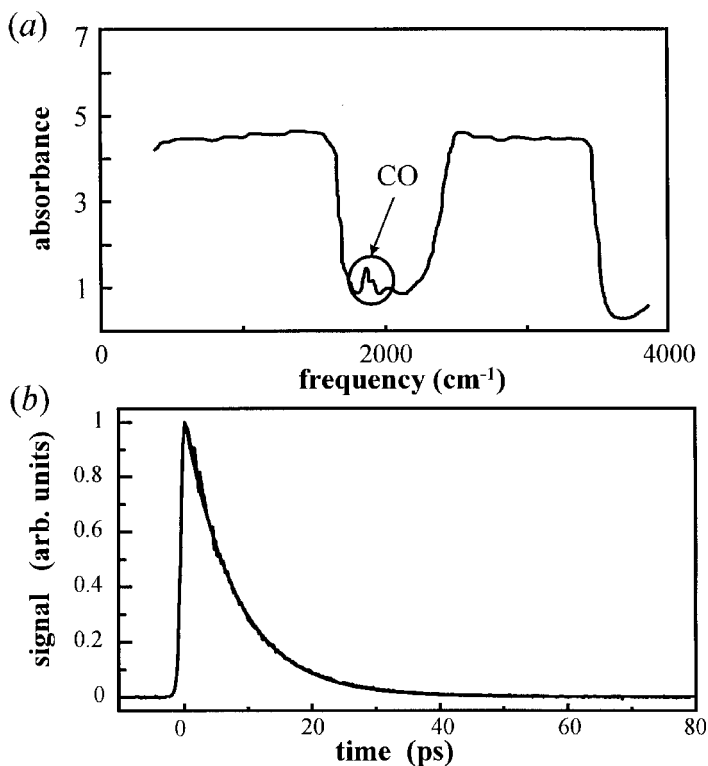
(a)

(b)

Figure 15.   (*a*) IR absorption spectrum of Mb–CO in 95:5 glycerol:water. Essentially all light is absorbed away from the 5 μm window. Near 5 μm, the solvent and protein have a background OD of about unity. The small CO stretching mode peaks can be seen above this background. (*b*) Example vibrational echo data taken on Mb–CO in 95:5 glycerol:water at 60 K and an exponential fit are shown. Data of this high quality are possible even on complex molecules such as proteins.

the protein and not by direct coupling of the CO to the solvent dynamics. This was verified by a variety of experiments [90–92] including vibrational echo studies of Mb–CO in the solvents ethylene glycol and trehalose [93]. In all three solvents, the low-temperature dephasing behaviours are identical [93]. Not only is the temperature dependence $T^{1.3}$ in all three solvents, but also the actual values of T_2^* are identical at all temperatures below about 200 K. In addition, experiments discussed below on the mutant H64V show that a change in the Mb amino acid sequence in the pocket of the protein causes a change in the pure dephasing.

The low-temperature $T^{1.3}$ dependence of the CO pure dephasing on temperature is reminiscent of dephasing by the two-level system dynamics observed for $Rh(CO)_2acac$ and of many other observables in glasses [1, 3, 12, 49]. However, in the protein, the power-law temperature dependence extends to much higher temperatures than in conventional glasses. One possibility is that a protein acts like a glass at low temperatures. There have been indirect experiments that have suggested this possibility [90–92]. The power-law temperature dependence in glasses arises from the many different structural transitions that occur in a glass at low temperatures. Glasses have a very broad and complex distribution of two-level system energy splittings and barrier heights (see figure 9). The distribution is often referred to as an energy landscape. Proteins have also been discussed as having a complex energy landscape
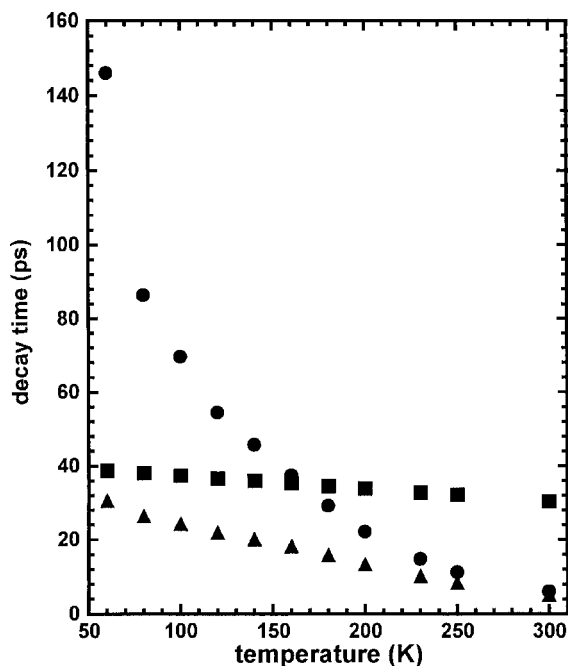
Figure 16.   Temperature-dependent data for native Mb–CO: ($\blacktriangle$), measured values of T_2 obtained from the vibrational echo decays using equation (6); ($\blacksquare$) $2T_1$ obtained from the decay constants measured in the pump–probe vibrational lifetime experiments; ($\bullet$), T_2^*, the pure dephasing times, obtained from T_2 and $2T_1$, using equation (2).
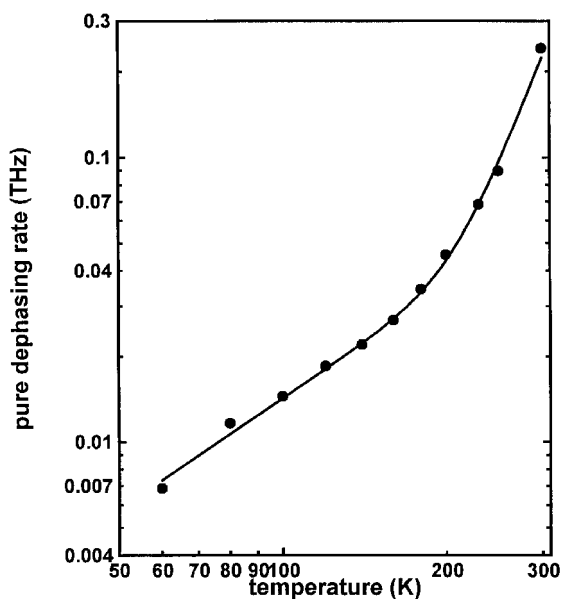

Figure 17.   Logarithmic plot of the pure dephasing rate $1/\pi T_2^*$ against temperature for native Mb–CO. Below about 200 K, the temperature dependence is dominated by a power law, $T^{1.3}$, which appears linear on the logarithmic plot. Above about 200 K, an exponentially activated process describes the data with $\Delta E \approx 1000$ cm^{-1}.

[90–92]. The $T^{1.3}$ temperature dependence can arise from tunnelling dynamics of a system of protein two-level systems [17, 18] which are akin to the two-level systems of very-low-temperature glasses. The same statistical mechanics machinery used to describe the low-temperature (about 1 K) heat capacities of glasses [94, 95] and the optical dephasing of electronic transitions of chromophores in low-temperature glasses [3] can be used to describe the protein two-level-system-induced vibrational dephasing of Mb–CO at much higher temperatures (below 200 K). A power-law temperature dependence can also arise from activation over barriers rather than tunnelling if there is the appropriate broad distribution of activation energies. In either case, the results suggest the existence of a complex protein energy landscape.

Near 200 K, there is a break in dephasing temperature dependence. This reflects a change to an exponentially activated process and is analogous to the change seen near 20 K in $Rh(CO)_2$acac in DBP. The low-temperature results in both cases appear to be similar. However, as stated above, for the $Rh(CO)_2$acac the exponentially activated process is the thermal activation of a single mode with strong coupling to the CO stretch. For Mb–CO, the high-temperature results are more complex.

Initially, it was proposed [93] that the break arose owing to the onset of the solvent's glass transition, which changed the possible motions of the protein surface. The glass transition for glycerol:water is about 180 K. However, recent unpublished experiments [93] disprove this hypothesis. A vibrational echo study of Mb–CO in trehalose, which as a glass transition above room temperature, also exhibits a break in the temperature dependence at about 200 K [93]. Therefore, the change in the temperature dependence involves properties of the protein and is not triggered by a glass transition of the solvent. In addition, a linear viscosity dependence of the Mb–CO vibrational dephasing has recently been observed [93]. These results suggest that the protein undergoes a transition from a glassy state to a more fluid-like state. In the fluid-like state, the protein can make transitions among a range of structural configurations that it either could not make or could only make at a very slow rate when in the glassy state. These transitions are activated processes with a narrow range of activation energies, giving the appearance of a single activation energy. The transitions require changes in the surface topology of the protein and, therefore, their rate is enhanced by a lower viscosity solvent. A detailed analysis of these results will be forthcoming [93].

5.2. *Coupling of protein fluctuations to the CO ligand at the active site*

For vibrational dephasing of CO bound to the active site of Mb to occur, the structural dynamics of the protein must be coupled to the vibrational states of the CO in a manner that causes fluctuations in the vibrational transition energy. Two models have been proposed to explain the dephasing in Mb [18]. One involves global electric field fluctuations and the other local mechanical coupling. In the global electric field model, motions of polar groups throughout the protein produce a time-dependent electric field. The fluctuating electric field causes modulation of the electron density of the haem's delocalized π-electron cloud. The haem π system is composed of the Fe d_π, N p_π and C p_π atomic orbitals. The CO bounded to the Fe is a σ donor of electron density to the haem. To alleviate excess charge density at the haem, there is a substantial back donation (back bonding) of haem π electron density to the CO π^* antibonding orbital. The back bonding causes a red shift of ν_{CO} because the electron density is donated to an antibonding orbital. It is well established from work on Mbs and other metal carbonyls [96–99] that changes in the back donation of electron

density into the CO π^* orbital are responsible for static shifts of the CO vibrational frequency. Furthermore, experiments [77] suggest that, in different Mbs, variations in electric fields resulting from different protein conformations are responsible for changes in back bonding and, therefore, observed static shifts in vibrational frequency [99, 100]. In this dephasing model, fluctuations of the haem π electron density modulate the magnitude of the back bonding to the CO π^* orbital, causing time-dependent shifts in ν_{CO}. These time-dependent shifts are responsible for the vibrational pure dephasing. In essence, the protein acts as a fluctuating electric field transmitter. The haem is an antenna which receives the signal of protein fluctuations and communicates it to the CO ligand bound at the active site.

In the local mechanical fluctuation model, the local motions of the amino acids on the proximal side of the haem are coupled to the haem through the side group of the proximal histidine. The proximal histidine is covalently bonded to the Fe. This bond is the only covalent bond of the haem to the rest of the protein. Thus, motions of the α-helix that contains the proximal histidine are directly coupled to the Fe. These motions can push and pull the Fe out of the plane of the haem. Since the CO is bound to the Fe, these motions may induce changes in the CO vibrational transition frequency, causing pure dephasing.

To test these models, we have performed a temperature-dependent vibrational echo and pump–probe study on two Mb mutants, H64V-CO and H93G(N-MeIm)–CO (N-MeIm = N-methylimidizole), both in 95:5 glycerol:water. These mutants were prepared using site-directed mutagenesis techniques [35, 36]. To test the global electric field model, we studied H64V, a Mb mutant in which the polar distal histidine is replaced by a non-polar valine. If the global electric field model of the dephasing is operative, then the decrease in the electric field in the mutant should reduce the magnitude of the frequency fluctuations, producing slower pure dephasing. To test the local mechanical model of pure dephasing, we studied H93G(N-MeIm), a Mb mutant in which the proximal histidine is replaced by a glycine. This severs the only covalent bond between the haem and the globin and leaves a large pocket on the proximal side of the haem. Inserted into this pocket and bound to the haem at the Fe is an exogenous N-MeIm, which has similar chemical properties to the side group of the histidine. Effectively, the proximal bond has been severed without changing significantly the electrostatic properties of the protein. If dynamics of the f α-helix are causing the pure dephasing by producing motions of the Fe via the proximal histidine, then the dephasing of this mutant should be less than that of the native protein.

Figure 18 shows the pure dephasing rates against temperature on a logarithmic plot of the native protein and the two mutants studied. The full circles represent the values for the native protein, which are the same as in figure 17. The full triangles are the pure dephasing rates for the mutant H93G(N-MeIm)–CO in 95:5 glycerol:water. Clearly, these values are identical with the native protein, indicating that the proposed local mechanical dephasing model is not active in myoglobin. The squares are the pure dephasing rates for the mutant H64V–CO in 95:5 glycerol:water. The data are fitted well with equation (9) using the same parameters as native; $\alpha = 1.3 \pm 0.1$ and $\Delta E = 1000 \pm 250$ cm^{-1}. However, the dephasing is $21 \pm 3\%$ slower than that of the native protein at all temperatures. The functional form of the temperature dependence is unchanged because modification of one amino acid does not significantly change the global dynamics of the protein. However, replacing the polar distal histidine with a non-polar valine removes one source of the fluctuating electric fields, reduces the coupling of the protein dynamics to the CO vibration and slows dephasing. These
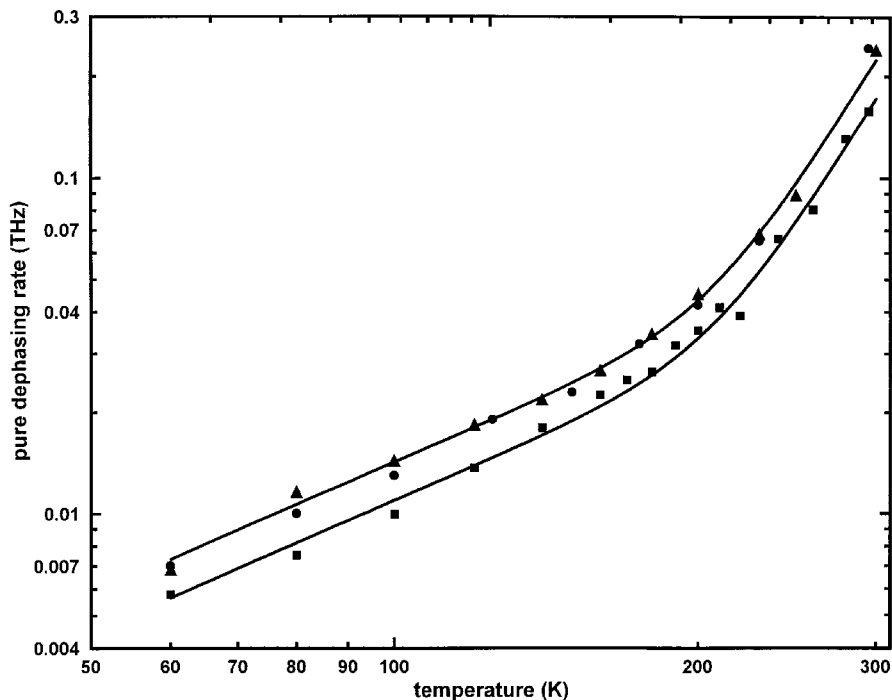
Figure 18.   Pure dephasing rate against temperature for native Mb–CO ($\bullet$) (same as figure 17). Also plotted is pure dephasing for H64V–CO ($\blacksquare$) and H93G(N-MeIm)–CO ($\blacktriangle$). As is clear, the native Mb–CO and the mutant H93G(N-MeIm)–CO have identical pure dephasing temperature dependences. The H64V–CO has an identical form of the pure dephasing but with a $21 \pm 3\%$ decrease in the pure dephasing rate at all temperatures studied.

results support the global electric field model of pure dephasing in Hb and suggest that the distal histidine contributes $21 \pm 3\%$ of the fluctuating electric fields felt at the haem. Recent molecular dynamics simulations [101] lend support to the approximately 20% electric field fluctuation produced by the distal histidine.

The reduced coupling of the protein to the haem is also evidenced by the change in the CO vibrational frequency in H64V compared with the dominant A_1 line of Mb. The A_1 line of Mb is at 1945 cm^{-1} while the H64V line is at 1969 cm^{-1}. The higher frequency is a result of the reduction in back bonding. In previous studies of the CO vibrational lifetimes T_1 of Mbs and model haem–CO compounds, it was found that there is a direct correlation between the CO absorption frequency and the vibrational lifetime [81, 91, 92, 102]. Higher vibrational transition frequencies were linearly associated with longer vibrational lifetimes. The lifetime results demonstrates that T_1 is determined by coupling of the CO vibration to the haem π-electron system via the back-bonding interaction. The vibrational relaxation does not occur via the Fe–CO σ bond as might be expected.

6.   Vibrational echo spectra

In this section, we present theoretical calculations and the first experimental data for a new vibrational spectroscopic technique, vibrational echo spectroscopy (VES) [29]. The VES technique can generate a vibrational spectrum with background suppression using the nonlinear vibrational echo pulse sequence. In contrast with the

previous results, VES is a utilization of vibrational echoes to measure spectra rather than dynamics.

Background suppression in VES is in some respects analogous to NMR background suppression techniques [103, 104]. In both types of spectroscopy, coherent sequences of pulses are used to remove unwanted spectral features. NMR and other magnetic resonance spectroscopies have had an enormous impact on the under-standing of molecular structure and dynamics in the last 50 years. The advent of the spin echo in 1950 [6], the first NMR coherent pulse technique, greatly enhanced the utility of NMR since the spin echo is the precursor of the sophisticated pulse techniques that were developed subsequently.

IR spectroscopy is inherently faster than NMR and can yield information about molecular motions and interactions in the femtosecond–nanosecond time ranges, while NMR yields information on far longer time scales. IR absorption spectroscopy has a much longer history, dating back to Newton's discovery of IR radiation in the early 1700s. IR absorption spectroscopy is a powerful technique for obtaining molecular structural information. In the region of the spectrum conventionally called the mid-IR, there are usually a large number of transitions, which arise from fundamental, overtone and combination band transitions. An absorption spectrum provides information about bonding, anharmonicity, solvent interactions and dynamics. However, even moderately sized molecules can generate spectra with a large number of peaks. For a large molecule, such as a protein, or a solute in a complex solvent, the spectrum may become so crowded that clean observation of the spectral feature of interest can become difficult. In principle, the solvent spectrum can be subtracted out by taking a background spectrum with the solvent alone. However, when the species of interest is in low concentration, accurately performing background subtraction is not trivial [105].

In complex molecular systems, such as proteins and other biological molecules, spectral bandwidths tend to be broad compared with the spacing between the bands. The spectral congestion produces broad features, which make structural assignments and quantitative IR absorption spectroscopy measurements difficult [78, 106]. There are a number of mathematical techniques that can narrow an absorption line [107]. However, the absorbance width and shape provides information on solute–solvent interactions and, possibly, dynamics, making pure mathematical line-narrowing techniques useful but not a perfect solution to the problem of congested spectra.

VES, as detailed below, can reduce or remove unwanted absorption and still return the line position, linewidth and line shape of the spectral features of interest under certain circumstances. However, because of the relative difficulty in obtaining ultrafast IR pulses, coherent pulsed IR spectroscopy in condensed-matter systems is a relatively new field.

In VES, line selectivity can be achieved because other overlapping transitions can have different homogeneous dephasing times of substantially different transition dipole moments. If the background absorption, which can be a broad, essentially continuous absorption of undesired peaks, has homogeneous dephasing times T_2^b (where the superscript b indicates background), short compared with the T_2 of the lines of interest, then VES can use the time evolution of the system to discriminate against the unwanted features. The time τ between the pulses in the vibrational echo sequence is set such that it is long compared with T_2^b but short compared with T_2. The vibrational echo signal from the background will have decayed to zero while the signal from the desired peaks will be non-zero. Scanning the IR wavelength of the vibrational echo

excitation pulses and detecting the vibrational echo signal will generate a spectrum in which the background is removed. If the background is composed of essentially a continuum of overtones and combination bands, while the peak of interest is a fundamental, it is likely that $T_2^b < T_2$.

It is also possible to discriminate against the background based on the relative strengths of the transitions even when $T_2^b \approx T_2$. Absorption is proportional to $m\mu^2$ while the vibrational echo signal is proportional to $m^2\mu^8$, where m is the concentration of the species and μ is the transition dipole matrix element. In a situation in which the background is composed of a high concentration of weak absorbers (m large and μ small) and the spectral features of interest are in low concentration but are strong absorbers (m small and μ large), the background absorption can overwhelm the desired features while the vibrational echo spectrum suppresses the background and reveals the relevant peaks. This situation can occur if the background arises from combination bands and overtones of the solvent while the relevant peaks are low-concentration fundamentals. An example such as this is presented below where the CO vibrational spectrum of Mb–CO is examined against a background of the protein and solvent absorptions.

6.1. *Vibrational echo spectroscopy theory*

Each spectral line can arise from a species with a particular concentration and transition dipole moment matrix element and a particular linewidth determined by the extent of homogeneous and inhomogeneous broadening. The magnitude of absorption as a function of frequency is given by Beer's law

$$A(\omega) = \sum_{i,j} \varepsilon_{ij}(\omega)\, m_i\, l, \tag{15}$$

where $A(\omega)$ is the absorption at frequency ω and $\varepsilon_{ij}(\omega)$ is the molar absorbtivity or the extinction coefficient of the jth transition of the ith species. ε has units of $M^{-1} cm^{-1}$ and is related to the transition dipole matrix element squared [108] m_i is the concentration of the ith species in the sample, and l is the length of the sample. For the jth transition of the ith species, the absorption is

$$A = \varepsilon_{ij} m_i l \propto |\mu^{ij}|^2 m_i l, \tag{16}$$

where μ^{ij} is the transition dipole matrix element of the jth transition of the ith species.

In a standard vibrational echo experiment, the wavelength of the IR light is fixed, and the delay τ between the excitation pulses is scanned. In VES, τ is fixed and the wavelength is scanned. To perform the VES calculation it is necessary to use a finite duration pulse, which has a finite bandwidth. In addition, the actual shape of the vibrational echo spectrum depends on the bandwidth of the laser pulse and the spectroscopic line shape. Several species with different concentrations, transition dipole moments, line shapes and homogeneous dephasing times can contribute to the signal. Therefore, VES calculations require determination of the nonlinear polarization using procedures that can accommodate these properties of real systems.

To calculate vibrational echo spectra, that is the vibrational echo intensity as a function of laser wavelength, including the details of the sample and laser pulses used in a real experiment, an efficient numerical algorithm for computing the vibrational echo signal for laser pulses of finite duration is employed [109]. In the experiment presented below, the pulse shapes are Gaussian; so the problem is considered for Gaussian pulses although the calculations can be performed for other pulse shapes.

The vibrational echo spectrum is calculated by numerically evaluating all the terms for the third-order nonlinear polarization $P^{(3)}$ that contribute to the signal in the vibrational echo geometry [109].

VES is possible even when T_2 is fast compared with the laser pulses since it is possible to have zero pulse delay, to scan the laser wavelength and to record the spectrum. To calculate the vibrational echo observable for a fixed laser frequency ω_1, $P^{(3)}$ must be integrated over the spectroscopic line, $g(\omega)$ or the laser bandwidth, whichever is narrower, and then the modulus squared of the result must be integrated over all time since the observable is the integrated intensity of the vibrational echo pulse:

$$I_s(\tau, \omega_1) \propto \int_{-\infty}^{\infty} dt_s \left| \int_0^{\infty} d\omega\, g(\omega)\, P_{\text{tot}}^{(3)}(\omega, t_s, \omega_1) \right|^2. \tag{17}$$

τ is the separation between the two laser pulses. The numerical calculation of the vibrational echo spectrum with realistic laser pulse envelopes and realistic material properties involves a five-dimensional integral. This is the situation for a single transition of a single species. In general, there are two or more spectroscopic lines with independent $P^{(3)}$. The contribution from each transition of each species must be summed at the polarization level and squared:

$$I_s(\tau, \omega_1) \propto \int_{-\infty}^{\infty} dt_s \left| \sum_{i,j} \left[\int_0^{\infty} d\omega^{i,j} g_{i,j}(\omega^{i,j})\, P_{\text{tot},i,j}^{(3)}(\omega^{i,j}, t_s, \omega_1) \right] \right|^2, \tag{18}$$

where i is the label for the species and j is the label for the jth transition of the ith species. It is necessary to distinguish between transitions on different species since the species may have different concentrations as well as the transitions having distinct line shapes $g_{i,j}(\omega^{i,j})$ and transition dipole matrix elements $\mu^{i,j}$.

In the calculations that are presented below, the laser pulse shapes and the inhomogeneous line shapes are Gaussian. The homogeneous line shapes are Lorentzians.

6.2. *Model calculation*

In this section, model calculations are presented to illustrate the T_2 contrast and transition dipole selection feature of VES. The calculations were performed using equation (18). While the VES line shape is not the same as that obtained from an absorption spectrum, it is possible to recover the absorption line shape from a vibrational echo spectrum. The same calculation procedures are applied to the experimental vibrational echo spectrum of the CO stretching mode of Mb–CO.

Figure 19 displays model calculations for a system with a high-OD solvent absorption and a narrow low-OD solute absorption. The abscissa is centred about the peak of the solute spectrum. Figure 19(a) is a model absorption spectrum. The parameters have been selected so that the broad solute absorption has a 100 times larger OD than the solute absorption has. The inset shows a magnified view of the solute absorption. Figures 19(b) and (c) show background-free vibrational echo spectra calculated using equation (18), which demonstrate two mechanisms for solvent background suppression. In figure 19(b) the spectrum is calculated with $\tau = 0$, and the suppression occurs because the solute has a large μ but low concentration relative to the solvent. The suppression arises from the $m^2\mu^8$ dependence of the vibrational echo spectrum against the $m\mu^2$ dependence of the absorption spectrum. This situation may be encountered frequently in real systems in which the peak of interest is a solute fundamental while the background consists of overtones and combination bands of
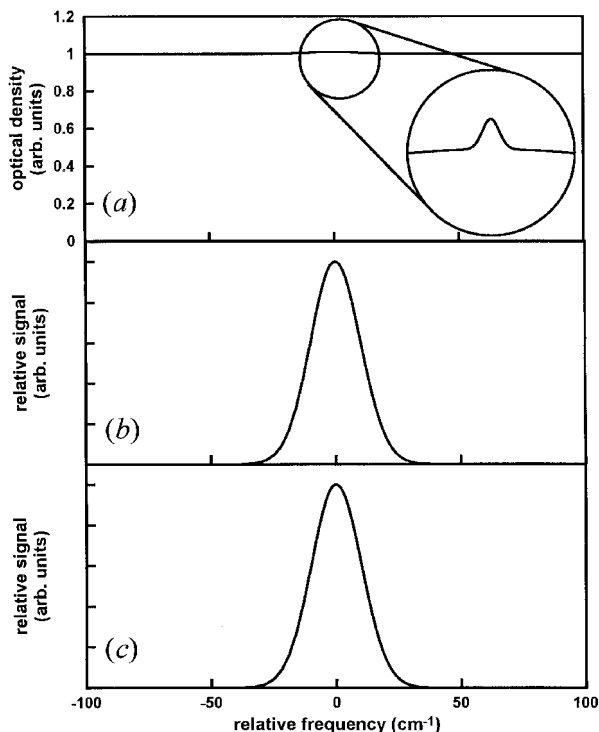
Figure 19.   Model calculations for a system with a broad high-OD solvent absorption and a narrow low-OD solute absorption. The abscissa is centred about the peak of the solute spectrum. (*a*) An absorption spectrum. The parameters have been selected so that the broad solute absorption has a 100 times larger OD than the solute absorption has. The inset shows a magnified view of the solute absorption. (*b*) (*c*) Background-free vibrational echo spectra demonstrating two mechanisms of solvent background suppression. (*b*) The spectrum is taken with $\tau = 0$, and the suppression occurs because the solute has a large μ but small concentration relative to the solvent. (*c*) An example of T_2 suppression. The solute and solvent μ and m were selected to give similar vibrational echo signals at $\tau = 0$. However, in this case, the solute $T_2 = 20$ ps and the solvent $T_2 = 0.1$ ps. The pulse delay is $\tau = 20$ ps. Because T_2 for the solvent is fast and T_2 for the solute is slow, the solvent vibrational echo decay is essentially complete while the solute vibrational echo signal is still significant. The result is background suppression based on the dynamics of the system rather than on the static properties of m and μ.

the solvent. In figure 19(*c*), an example of T_2 suppression is shown. The spectrum is calculated with $\tau = 20$ ps. The solvent has $T_2^b = 0.1$ ps and the solute has $T_2 = 20$ ps.

Figure 20 illustrates the nature of T_2 suppression by presenting vibrational echo spectra for two spectral lines with different T_2 values as a function of delay time. One of the lines has a very short $T_2^b = 0.1$ ps and a broad inhomogeneous linewidth. This broad line contributes the vast majority of the signal (about 99%) at $\tau = 0$ because of the values used for the parameters μ and m. The other line has a significantly longer $T_2 = 1.0$ ps and a narrower inhomogeneous linewidth. For both absorption bands, the inhomogeneous linewidths are large compared with the homogeneous linewidths. The absorption spectrum would show only a single broad line. The four curves displayed in figure 20 are vibrational echo spectra calculated for four different delay times τ. Each of the four curves has been scaled so that it has the same height at line centre although the maximum magnitude of the spectrum decreases as τ increases. The top
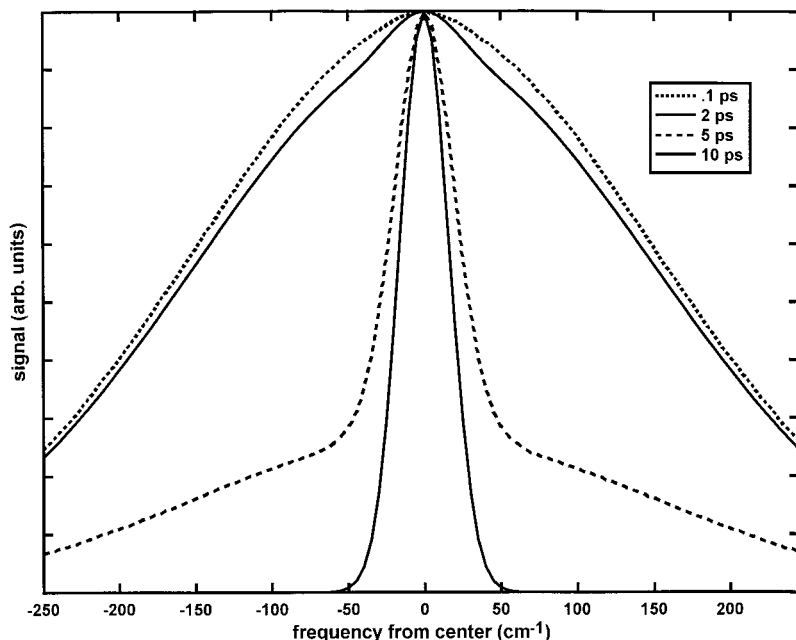
Figure 20. Calculations to illustrate T_2 contrast. The system is composed of two Gaussians. The 'solvent' Gaussian has an amplitude of about unity, an inhomogeneous width of 500 cm^{-1} and a T_2 of 0.1 ps. the 'chromophore' Gaussian has an amplitude of 0.01, an inhomogeneous width of 50 cm^{-1} and a T_2 of 1.0 ps. The centre frequencies of both are the same. The lines illustrate a variety of delays between the two echo pulses. At a delay of 0.1 ps, VES shows the massive 'solvent' peak with a small bump of the 'chromophore'. By extending the delay to 2 and 5 ps, the 'solvent' contribution becomes less and less significant. At 10 ps, the solvent contribution is gone and only the chromophore VES is shown. Spectra are normalized.

(dotted) curve is the calculated vibrational echo spectrum at $\tau = 0.1$ ps. The spectrum is essentially the spectrum of the fast T_2 line. The next (upper solid) curve is calculated with $\tau = 2$ ps. The influence of the slower T_2 line is becoming visible. At this delay time, the polarization generated by the fast T_2 line has dropped while the polarization generated by the slow T_2 line is almost unchanged. In the next (broken) curve ($\tau = 5$ ps), the signal from the fast T_2 line is smaller than that of the slow T_2 line. Finally, in the last (lower solid) curve ($\tau = 10$ ps), the polarization produced by the fast T_2 line is virtually zero. While the vibrational echo signal from the slow T_2 line is reduced, this narrow inhomogeneous line now totally dominates the spectrum. This is an idealized example in which the differences in T_2 are large enough that the unwanted line can be completely suppressed. If the T_2 values are not too different, a spectrum such as the third curve may be produced. The buried line is revealed and the background is partially suppressed. Considerable information can be extracted from such a spectrum. It is possible to determine the absorption line shape from VES data. The result is background suppression based on the dynamics of the system rather than on the static properties of m and μ. If the peak of interest is a fundamental of the solute while the background is basically a continuum of overtone and combination bands of the solvent, T_2 suppression can be viable, particularly at reduced temperature. T_2 suppression of the background is equivalent to T_2 image enhancement in magnetic resonance imaging.

6.3. *Experimental demonstration of vibrational echo spectroscopy*

VES requires a tunable source of IR pulses. This can be provided by conventional laser systems using optical parametric amplifiers (OPAs) to down-convert visible or near-IR light into the mid-IR region necessary to perform vibrational spectroscopy. In the experiments presented below on Mb–CO, vibrational echo spectra were taken using the Stanford FEL and the same experimental set-up used to carry out the decay experiments discussed above [17]. VES measurements were made at a number of fixed frequency points rather than continuously scanning the FEL. The data collection at fixed points was necessary because of the current configuration of the FEL. In the future, it should be possible to scan the FEL continuously, and it is also possible to scan OPA-based systems continuously. Therefore, future VES experiments may be performed in a manner analogous to other laser spectroscopy experiments with continuous scanning of the frequency. The absolute signal for each point at a fixed τ was recorded. Each point was normalized by the laser intensity cubed I^3. This is the simple normalization constant assuming no inner filter effect. The inner filter effect will be discussed in detail in a full treatment of VES [29].

The first VES experiments were conducted on CO bound to Mb in the solvent mixture of 95:5 glycerol:water. Figure 21(*a*) displays the absorption spectrum of Mb–CO in the region of the CO stretch transition. The CO peaks at about 1950 cm^{-1} are on top of a background with an OD of about unity. The A_1 peak is the largest peak with the A_0 peak barely discernible. A_3 cannot be seen in this spectrum, but it has been observed in different types of sample [88, 110]. The A_1 peak has an OD of about 0.2 above the background. The background is composed of both protein and solvent absorptions. To obtain a CO spectrum that is clearly visible above the background, it is necessary to prepare a sample with a high concentration of protein (15–20 mM) in a short-path-length (125 μm) cell to reduce the contribution to the background from the solvent. Since there is one CO per protein molecule, the background arising from the protein cannot be reduced.

Figure 21(*b*) displays VES data for Mb–CO together with a theoretical calculation of the vibrational echo spectrum. The full circles are the data. The spectrum was taken point by point. The amplitude of each point was determined from the magnitude of the vibrational echo signal at zero delay ($\tau = 0$). The square root of the vibrational echo spectrum is presented for direct comparison with the absorption spectrum. As discussed above, the vibrational echo spectrum at the polarization level is directly related to the absorption spectrum. The height of the spectrum has been scaled to unity. Note that the vibrational echo spectrum has zero background. The protein and solvent do not contribute to the vibrational echo spectrum in the vicinity of 1950 cm^{-1} although they dominate the absorption spectrum. The vibrational echo spectrum displayed no background even at $\tau = 0$, indicating that the selectivity arises from differences in transition moments rather than in the T_2 values. The width of the vibrational echo spectrum is wider than the absorption spectrum because the bandwidth of the laser (13 cm^{-1}) is comparable with the spectral linewidth. Like any spectroscopic measurement, if the instrument resolution function is comparable with the linewidth, the spectrum will be broadened.

The solid curve in figure 21(*b*) is the calculated vibrational echo spectrum using the procedures outlined in the section above. The spectrum was modelled as having three independent transitions at different centre frequencies but with the same homogeneous widths, inhomogeneous widths and transition dipole moments as the A_1 state. The homogeneous width of A_1 was determined using a vibrational echo decay. The
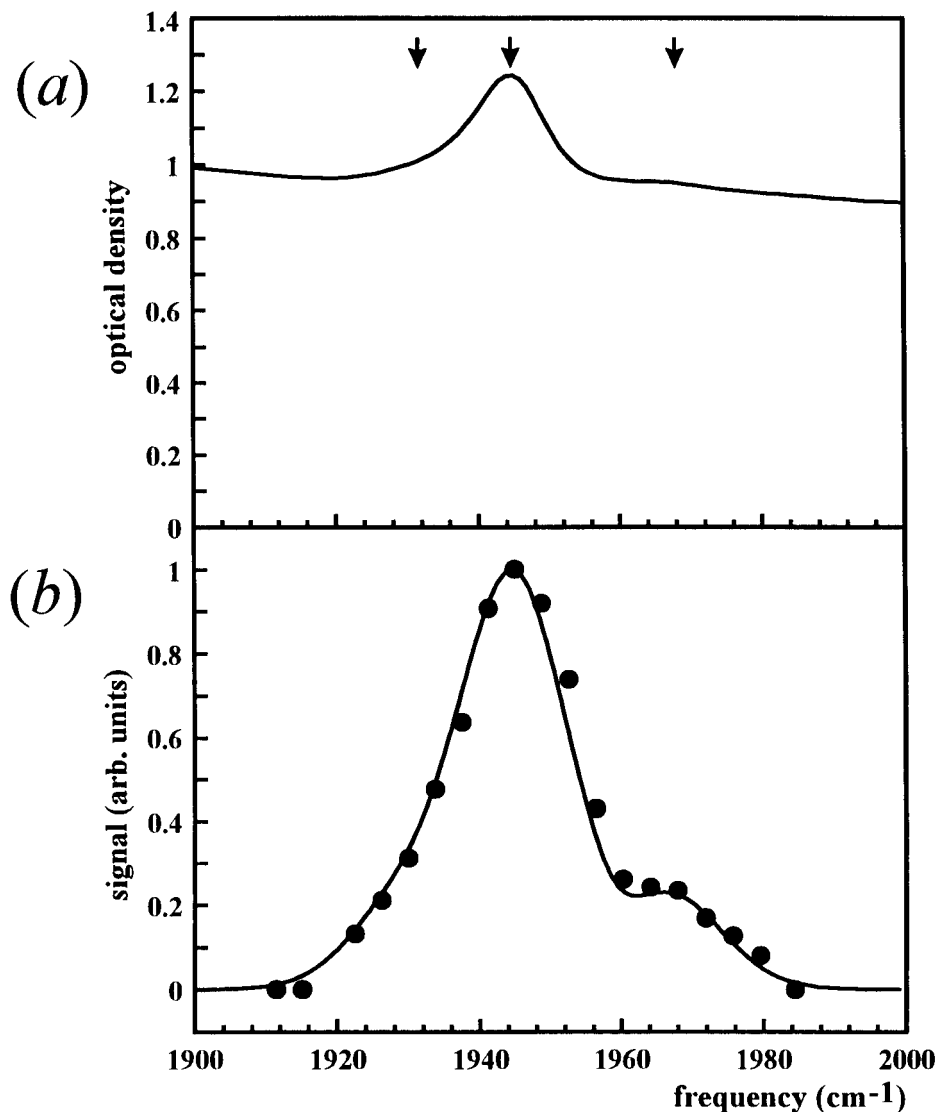
Figure 21. (*a*) Absorption spectrum of Mb–CO in the region of the CO stretching mode. Only the A_1 conformer is clearly discernible. The spectrum has a background (solvent+ protein) OD of about unity. (*b*) Example of VES data and fit: (●), square root of the experimental vibrational echo intensities at zero fixed delay with the laser wavelength varied. See text for details of the calculation.

vibrational echo decay experiments show that the linewidth is dominated by inhomogeneous broadening. The absorption linewidth of the A_1 peak was determined from the absorbance spectra. There is some uncertainty in this width because of the overlapping lines and the large background absorption. The centre frequencies of the three transition used in the calculation are those reported in the literature [82, 110] and given above. The pulse duration and spectral width and shape of the laser pulses are known from autocorrelations and spectra. Like the data, the solid curve is the square root of the calculated vibrational echo spectrum. As can be seen, the calculation matches the experimental results quite well. It appears that a small shift in the data to

higher energy would improve the agreement. This might be caused by a calibration error in the determination of the FEL wavelength. While the A_3 line is not visible as a distinct peak, it was found that, without including it in the calculation, the high-energy side of the calculated spectrum fell off much faster than the data. Also note that the A_0 line is more prominent in the VES spectrum than in the absorption spectrum. As will be discussed in another publication [29], T_2 selectivity enhances this peak relative to A_1.

While the Mb–CO spectrum can be taken with conventional IR absorption spectroscopy, the VES results demonstrate the potential of using VES to enhance vibrational spectra and potentially to observe peaks that are completely lost in a broad, highly absorbing background. The many powerful pulses sequences used in NMR to enhance spectra have been developed over a number of decades. The VES results may be the precursor to an equivalent approach, using coherent pulse sequences in vibrational spectroscopy.

7. Concluding remarks

Vibrational echo experiments have made it possible to perform a detailed examination of the dynamics of intermolecular and intramolecular interactions that give rise to the homogeneous linewidths and pure dephasing of the asymmetric CO stretching modes of $Rh(CO)_2acac$ and $W(CO)_6$ in liquid and glassy solvents and of the stretching mode of CO bound at the active site of Mb proteins. Even when $Rh(CO)_2acac$ and $W(CO)_6$ are in the same solvent, the functional forms of their temperature-dependent pure dephasing are different. At low temperature (from 3.5 to about 20 K), $Rh(CO)_2acac$ pure dephasing goes as T. This is interpreted as the result of coupling of the vibrational mode of the dynamical two-level systems of the glassy DBP solvent. Above about 20 K, the pure dephasing becomes exponentially activated with an activation energy of about 400 cm^{-1}. There is no change in the functional form of the temperature dependence in passing from the glass to the liquid. These results suggest that the activated process arises from coupling of the high-frequency CO stretch to the internal 405 cm^{-1} Rh–C asymmetric stretching mode. Excitation of the Rh–C stretch produces changes in the back donation of electron density from the metal d_π orbitals to the CO π^* antibonding orbital, shifting the CO stretching transition frequency and causing pure dephasing.

The pure dephasing of $W(CO)_6$ has a T^2 temperature dependence in DBP, 2MP and 2MTHF glasses. In all three solvents, there is an abrupt change in the functional form of the temperature dependence in going from the glass to the liquid. In liquid 2MP, the pure dephasing has a VTF temperature dependence. The major differences in the temperature-dependent pure dephasing of the asymmetric stretching modes of $Rh(CO)_2acac$ and $W(CO)_6$ are attributed to the difference in the degeneracy of the modes. The $Rh(CO)_2acac$ mode is non-degenerate while the $W(CO)_6$ mode is triply degenerate in the gas phase. When $W(CO)_6$ is placed in a glass or liquid solvent, the local anisotropic solvent structure beaks the degeneracy, yielding three modes with small energy splittings. The results indicate that these splittings are very sensitive to local fluctuations in the solvent, giving rise to dephasing mechanisms that are not available to $Rh(CO)_2acac$. The abrupt change in the temperature dependence of the $W(CO)_6$ vibrational pure dephasing above T_g occurs because the nature of the local solvent structural fluctuations changes in going from a glass to a liquid.

The vibrational echo experimental results presented on the metal carbonyls provide increased understanding of the dynamics that lead to vibrational energy level

fluctuations. Vibrational echo experiments are also a probe of solvent dynamics. It is interesting and useful to note that the two molecules studied provide probes of different aspects of solvent dynamics. At low temperatures, the vibrational pure dephasing of $Rh(CO)_2acac$ is sensitive to the glass's structural evolution produced by two-level system dynamics, while that of $W(CO)_6$ is not. However, above T_g, the broken degeneracy of the T_{1u} mode of $W(CO)_6$ causes its vibrational pure dephasing to be sensitive to the dynamics of the supercooled liquid, while the non-degenerate mode of $Rh(CO)_2acac$ is not.

Vibrational echo experiments have also been applied to the CO stretching mode of Mb–CO and mutant Mb proteins. Vibrational echo and lifetime measurements have been made on CO bound to the active site of native Mb, H64V, a mutant of Mb with the distal histidine replaced with a valine, and H93G(N-MeIm), a mutant of Mb with the proximal histidine replaced with a glycine and exogenous N-MeIm bound at the Fe in the proximal pocket. Combining the results of the vibrational echo with pump–probe data, the pure dephasing times T_2^* have been measured at a series of temperatures from 60 to 300 K. T_2^* is a measure of the vibrational energy level fluctuations induced by conformational fluctuations of the protein. The vibrational lines are inhomogeneously broadened at all temperatures in this range. Thus, even at room temperature, the ensemble of protein molecules exists in a distribution of conformational substates that interconvert slowly compared to the tens-of-pico-seconds time scale of the vibrational echo experiment. The fact that the absorption spectra are inhomogeneously broadened means that dynamical information cannot be extracted from the absorption spectra.

The temperature-dependent vibrational echo results show that the pure dephasing of H64V is about $21 \pm 3\%$ slower than that of native Mb with no change in the functional form of the temperature dependence. The temperature dependence of the pure dephasing of H93G(N-MeIm) is identical with that of the native Mb. The general mechanism proposed [17] to explain the coupling of conformational fluctuations of the protein to the vibrational transition energy of CO bound at the active site is supported by the H64V results. The model states that protein motions produce fluctuating electric fields which are responsible for the CO pure dephasing. Replacing the polar distal histidine with the non-polar valine removes one source of the fluctuating electric fields, thus reducing the coupling between the protein fluctuations and the measured pure dephasing. The picture that emerges is that the haem acts as an antenna that receives and then communicates protein fluctuations to the vibration of the CO ligand bound at the active site.

Vibrational echo data obtained on H93G(N-MeIm) in which the single covalent linkage between haem–CO and the protein is broken show that the temperature dependence of the vibrational pure dephasing is identical with that of native Mb. The experiments demonstrate that local mechanical motions of the proximal histidine which directly couple the Fe to the fluctuations of the globin are not responsible for vibrational pure dephasing of CO bound at the active site of Mb.

Two spectroscopic applications of vibrational echoes were also presented. The VEB experiment was used to measure the anharmonicity of the vibrational potential. VEB can also be used to extract dynamical information for transitions other than $v = 0$–1 [30, 31]. The vibrational echo spectrum method was also described and demonstrated. In the VES technique, the delay between the two pulses is fixed and the laser frequency is scanned across the transition of interest. The VES technique can selectively remove unwanted spectral features, such as a broad background ab-

sorption, using differences in either homogeneous dephasing or transition dipole moments. The method was demonstrated on the CO stretching transitions of Mb–CO near 1950 cm^{-1} by suppressing the protein and high-OD background absorption.

The ultrafast IR vibrational echo experiment is a powerful new technique for the study of molecules and vibrational dynamics in condensed-matter systems. In 1950, the advent of the NMR spin echo [6] was the first step on a road that has led to the incredibly diverse applications of NMR in many fields of science and medicine. Although vibrational spectroscopy has existed far longer than NMR, the experiments described here are the first ultrafast resonant vibrational analogues of pulsed NMR methods. In the future, it is anticipated that the vibrational echo will be extended to an increasingly diverse range of problems and that the technique will be expanded to new pulse sequences including multidimensional coherent vibrational spectroscopies.

References

[1] THIJSSEN, H. P. H., DICKER, A. I. M., and VÖLKER, S., 1982, *Chem. Phys. Lett.*, **92**, 7.
[2] HARRER, D., 1988, *Photochemical Hole-Burning in Electronic Transitions* (Berlin: Springer).
[3] NARASIMHAN, L. R., LITTAU, K. A., PACK, D. W., BAI, Y. S., ELSCHNER, A., and FAYER, M. D., 1990, *Chem. Rev.*, **90**, 439.
[4] FEI, S., YU, G. S., LI, H. W., and STRAUSS, H. L., 1996, *J. chem. Phys.*, **104**, 6398.
[5] TOKMAKOFF, A., URDAHL, R. S., ZIMDARS, D., FRANCIS, R. S., KWOK, A. S., and FAYER, M. D., 1994, *J. chem. Phys.*, **102**, 3919.
[6] HAHN, E. L., 1950, *Phys. Rev.*, **80**, 580.
[7] KURNIT, N. A., ABELLA, I. D., and HARTMANN, S. R., 1964, *Phys. Rev. Lett.*, **13**, 567.
[8] ABELLA, I. D., KURNIT, N. A., and HARTMANN, S. R., 1966, *Phys. Rev. Lett.*, **14**, 391.
[9] GORDON, R. G., 1965, *J. chem. Phys.*, **43**, 1307.
[10] GORDON, R. G., 1968, *Adv. Magn. Reson.*, **3**, 1.
[11] BERNE, B. J. 1971, *Physical Chemistry: An Advanced Treatise* (New York: Academic Press).
[12] MOLENKAMP, L. W., and WIERSMA, D. A., 1985, *J. chem. Phys.*, **83**, 1.
[13] VAINER, Y. G., PERSONOV, R. I., ZILKER, S., and HAARER, D., 1996, *Proceedings of the Fifth International Meeting on Hole Burning and Related Spectroscopies: Science and Applications*, Vol. 291, edited by G. J. Small (Brainerd, Minnosota: Gordon and Breach), p. 51.
[14] BERG, M., WALSH, C. A., NARASIMHAN, L. R., LITTAU, K. A., and FAYER, M. D. 1988, *J. chem. Phys.*, **88**, 1564.
[15] TOKMAKOFF, A., ZIMDARS, D., URDAHL, R. S., FRANCIS, R. S., KWOK, A. S., and FAYER, M. D., 1995, *J. phys. Chem.*, **99**, 13310.
[16] TOKMAKOFF, A., and FAYER, M. D., 1995. *J. chem. Phys.* **102**, 2810.

[17] RELLA, C. W., RECTOR, K. D., KWOK, A. S., HILL, J. R., SCHWETTMAN, H. A., DLOTT, D. D., and FAYER, M. D., 1996, *J. phys. Chem.*, **100**, 15620.
[18] RECTOR, K. D., RELLA, C. W., KWOK, A. S., HILL, J. R., SLIGAR, S. G., CHIEN, E. Y. P., DLOTT, D. D., and FAYER, M. D., 1997, *J. phys. Chem.* B, **101**, 1468.
[19] RECTOR, K. D., ENGHOLM, J. R., RELLA, C. W., HILL, J. R., HU, R., BOXER, S. G., DLOTT, D. D., and FAYER, M. D., 1998, *J. phys. Chem. B*, **102**, 331 .
[20] YAN, Y. J., and MUKAMEL, S., 1991, *J. chem. Phys.*, **94**, 179.
[21] MUKAMEL, S., 1995, *Principles of Nonlinear Optical Spectroscopy* (Oxford University Press).
[22] FARRAR, T. C., and BECKER, D. E., 1971, *Pulse and Fourier Transform NMR* (New York: Academic Press).
[23] SKINNER, J. L., ANDERSON, H. C., and FAYER, M. D., 1981, *J. chem. Phys.*, **75**, 3195.
[24] SCHWEIZER, K. S., and CHANDLER, D., 1982, *J. chem. Phys.*, **76**, 2240.
[25] OXTOBY, D. W., 1981, *A. Rev. phys. Chem.*, **32**, 77.
[26] TOKMAKOFF, A., URDAHL, R. S., ZIMDARS, D., KWOK, A. S., FRANCIS, R. S., and FAYER, M. D., 1995, *J. chem. Phys.*, **102**, 3919.
[27] LORING, R. F., and MUKAMEL, S., 1985, *J. chem. Phys.*, **83**, 2116.
[28] BAI, Y. S., and FAYER, M. D., 1989, *Phys. Rev.* B, **39**, 11066.
[29] RECTOR, K. D., ZIMDARS, D. A., and FAYER, M. D., 1998, *J. chem. Phys.* (submitted).
[30] RECTOR, K. D., KWOK, A. S., FERRANTE, C., TOKMAKOFF, A., RELLA, C. W., and FAYER, M. D., 1997, *J. chem. Phys.*, **106**, 10027.
[31] TOKMAKOFF, A., KOWK, A. S., URDAHL, R. S., FRANCIS, R. S., and FAYER, M. D., 1995, *Chem. Phys. Lett.*, **234**, 289.
[32] MUKAMEL, S., and LORING, R. F., 1986, *J. opt. Soc. Am.* B, **3**, 595.
[33] BAI, Y. S., GREENFIELD, S. R., FAYER, M. D., SMITH, T. I., FRISCH, J. C., SWENT, R. L., and SCHWETTMAN, H. A., 1991, *J. Opt. Soc. Am.* B, **8**, 1652.
[34] SCHWETTMAN, H. A., 1996, *Nucl. Instrum. Meth.* **A, 375**, 632.
[35] SPRINGER, B. A., and SLIGAR, S. G., 1987, *Proc. natln. Acad. Sci. USA*, **84**, 8961.
[36] DECATUR, S. M., DEPILLIS, G. D., and BOXER, S. G., 1996, *Biochemistry*, **35**, 3925.
[37] RECTOR, K. D., and FAYER, M. D., 1998, *J. chem. Phys.*, **108**, 1794.
[38] RECTOR, K. D., KWOK, A. S., FERRANTE, C., FRANCIS, R. S., and FAYER, M. D., 1997, *Chem. Phys. Lett.*, **276**, 217.
[39] ANGELL, C. A., 1982, *J. phys. Chem.*, **86**, 3845.
[40] ANGELL, C. A., 1988, *J. Phys. Chem. Solids*, **49**, 863.
[41] FREDRICKSON, G. H., 1988, *A. Rev. phys. Chem.*, **39**, 149.
[42] LEE, H. W. H., HUSTON, A. L., GEHRTZ, M., and MOERNER, W. E., 1985, *Chem. Phys. Lett.*, **114**, 491.
[43] HAYES, J. M., STOUT, R. P., and SMALL, G. J., 1981, *J. chem. Phys.*, **74**, 4266.
[44] MACFARLANE, R. M., and SHELBY, R. M., 1983, *Optics Commun.*, **45**, 46.
[45] MACFARLANE, R. M., and SHELBY, R. M., 1987, *J. Lumin.*, **36**, 179.
[46] FRIEDRICH, J., WOLFRUM, H., and HAARER, D., 1982, *J. chem. Phys.*, **77**, 2309.
[47] PHILLIPS, W. A., 1972, *J. low Temp. Phys.*, **7**, 351.
[48] ANDERSON, P. W., HALPERIN, B. I., and VARMA, C. M., 1972, *Phil. Mag.*, **25**, 1.
[49] HAYES, J. M., JANKOWIAK, R., and SMALL, G. J., 1988, *Persistent Spectral Hole Burning: Science and Applications*, edited by W. E. Moerner (Berlin: Springer), p. 153.
[50] GEVA, E., and SKINNER, J. L., 1997, *J. chem. Phys.*, **107**, 7630.
[51] KASSNER, K., and SILBEY, R., 1989, *J. Phys.* C, **1**, 4599.
[52] SELZER, P. M., HUBER, D. L., HAMILTON, D. S., YEN, W. M., and WEBER, M. J., 1976, *Phys. Rev. Lett.*, **36**, 813.
[53] ELSCHNER, A., NARASIMHAN, L. R., and FAYER, M. D., 1990, *Chem. Phys. Lett.*, **171**, 19.
[54] GREENFIELD, S. R., BAI, Y. S., and FAYER, M. D., 1990, *Chem. Phys. Lett.*, **170**, 133.
[55] KITAIGORODSKY, A. I., 1973, *Molecular Crystals and Molecules* (New York: Academic Press).
[56] HSU, D., and SKINNER, J. L., 1985, *J. chem. Phys.*, **83**, 2097.
[57] SHELBY, R. M., HARRIS, C. B., and CORNELIUS, P. A., 1978, *J. chem. Phys.*, **70**, 34.
[58] ADAMS, D. M., and TRUMBLE, W. R., 1974, *J. chem. Soc.*, *Dalton Trans.*, 690.
[59] ADAMS, D. M., 1968, *Metal–Ligand and Related Vibrations* (New York: St Martin's Press).
[60] JONES, L. H., MCDOWELL, R. S., and GOLDBLATT, M., 1969, *Inorg. Chem.*, **8**, 2349.

[61] STRATT, R. M., 1995, *Accts Chem. Res.*, **28**, 201.
[62] KEYES, T., 1997, *J. phys. Chem.* A, **101**, 2921.
[63] CHANG, Y. J., and CASTNER, E. W., JR, 1996, *J. phys. Chem.*, **100**, 3330.
[64] ARRIVO, S. M., DOUGHERTY, T. P., GRUBBS, W. T., and HEILWEIL, E. J., 1995, *Chem. Phys. Lett.*, **235**, 247.
[65] OWRUTSKY, J. C., LI, M., LOCKE, B., and HOCHSTRASSER, R. M., 1995, *J. phys. Chem.*, **99**, 4842.
[66] FOURKAS, J. T., KAWASHIMA, H., and NELSON, K. A., 1995, *J. chem. Phys.*, **103**, 4393.
[67] ZHU, X., HYBERTSEN, M. S., LITTLEWOOD, P. B., and NUSS, M. C., 1994, *Phys. Rev.* B, **50**, 11 915.
[68] CUNDIFF, S. T., 1994, *Phys. Rev.* A, **49**, 3114.
[69] FOURKAS, J., 1996, private communication.
[70] KURIYAN, J. W., KARPLUS, M., and PETSKO, G. A., 1986, *J. molec. Biol.*, **192**, 133.
[71] QUILLIN, M. L., ARDUINI, R. M., OLSON, J. S., and PHILLIPS, G. N., JR, 1993, *J. molec. Biol.*, **234**, 140.
[72] BARRICK, D., 1994, *Biochemistry*, **33**, 6546.
[73] HAVEL, H. A., 1996, *Spectroscopic Methods for Determining Protein Structure in Solution* (New York: VCH).
[74] BRAUNSTEIN, D. P., CHU, K., EGEBERG, K. D., FRAUENFELDER, H., MOURANT, J. R., NIENHAUS, G. U., ORMOS, P., SLIGAR, S. G., SPRINGER, B. A., and YOUNG, R. D., 1993, *Biophys. J.*, **65**, 2447.
[75] JACKSON, T. A., LIM, M., and ANFINRUD, P. A., 1994, *Chem. Phys.*, **180**, 131.
[76] JANES, S. M., DALICKAS, G. A., EATON, W. A., and HOCHSTRASSER, R. M., 1988, *Biophys. J.*, **54**, 545.
[77] OLDFIELD, E., GUO, K., AUGSPURGER, J. D., and DYKSTRA, C. E., 1991, *J. Am. chem. Soc.*, **113**, 7537.
[78] SUREWICZ, W. K., and MANTSCH, H. H., 1996, *Spectroscopic Methods for Determining Protein Structure in Solution*, edited by H. A. Havel (New York: VCH), pp. 135–162.
[79] ELBER, R., and KARPLUS, M., 1987, *Science*, **235**, 318.
[80] LEESON, D. T., and WIERSMA, D. A., 1995, *Phys. Rev. Lett.*, **74**, 2138.
[81] HILL, J. R., DLOTT, D. D., RELLA, C. W., PETERSON, K. A., DECATUR, S. M., BOXER, S. G., and FAYER, M. D., 1996, *J. phys. Chem.*, **100**, 12 100.
[82] HILL, J. R., DLOTT, D. D., RELLA, C. W., SMITH, T. I., SCHWETTMAN, H. A., PETERSON, K. A., KWOK, A. S., RECTOR, K. D., and FAYER, M. D., 1996, *Biospec.*, **2**, 227.
[83] DEBRUNNER, P. G., and FRANUENFELDER, H., 1982, *Rev. phys. Chem.*, **33**, 283.
[84] FRAUENFELDER, H., PARAK, F., and YOUNG, R. D., 1988, *A. Rev. Biophys. biophys. Chem.*, **17**, 471.
[85] PETRICH, J. W., and MARTIN, J. L., 1989, *Time-Resolved Spectroscopy*, edited by R. J. H. Clark and R. E. Hester (New York: Wiley), p. 335.
[86] FRIEDMAN, J. M., ROUSSEAU, D. L., and ONDRIAS, M. R., 1982, *A. Rev. phys. Chem.*, **33**, 471.
[87] STRYER, L., 1988, *Biochemistry*, third edition (New York: W. H. Freeman).
[88] ANSARI, A., BEREDZEN, J., BRAUNSTEIN, D., COWEN, B. R., FRAUENFELDER, H., HONG, M. K., IBEN, I. E. T., JOHNSON, J. B., ORMOS, P., SAUKE, T., SCHROLL, R., SCHULTE, A., STEINBACK, P. J., VITTITOW, J., and YOUNG, R. D., 1987, *Biophys. Chem.*, **26**, 337.
[89] IBEN, I. E. T., BASUNSTEIN, D., DOSTER, W., FRAUENFELDER, H., HONG, M. K., JOHNSON, J. B., LUCK, S., ORMOS, P., SCHULTE, A., STEINBACK, P. J., XIE, A., and YOUNG, R. D., 1989, *Phys. Rev. Lett.*, **62**, 1916.
[90] HILL, J. R., TOKMAKOFF, A., PETERSON, K. A., SAUTER, B., ZIMDARS, D. A., DLOTT, D. D., and FAYER, M. D., 1994, *J. phys. Chem.*, **98**, 11 213.
[91] HILL, J. R., ROSENBLATT, M. M., ZIEGLER, C. J., SUSLICK, K. S., DLOTT, D. D., RELLA, C. W., and FAYER, M. D., 1996, *J. phys. Chem.*, **100**, 18 023.
[92] HILL, J. R., DLOTT, D. D., FAYER, M. D., RELLA, C. W., ROSENBLATT, M. M., SUSLICK, K. S., and ZIEGLER, C. J., 1996, *J. phys. Chem.*, **100**, 218.
[93] RECTOR, K. D., DLOTT, D. D., and FAYER, M. D., 1998 (to be published).
[94] PHILLIPS, W. A., 1981, *Amorphous Solids. Low Temperature Properties*, Topics in Current Physics (Berlin: Springer).

[95] STEVELS, J. M., 1962, *Thermodynamics of Liquids and Solids*, edited by S. Flügge (Berlin: Springer), p. 13.

[96] COTTON, F. A., and WILKINSON, G., 1988, *Advanced Inorganic Chemistry* (New York: Wiley–Interscience).

[97] BOLDT, N. J., GOODWILL, K. E., and BOCIAN, D. F., 1988, *Inorg. Chem.*, **27**, 1188.

[98] SPIRO, T. G., 1983, *Iron Porphyrins* (Reading, Massachusetts: Addison-Wesley).

[99] LI, X. Y., and SPIRO, T. G., 1988, *J. Am. chem. Soc.*, **110**, 6024.

[100] PARK, K. D., GUO, K., ADEBODUN, F., CHIU, M. L., SLIGAR, S. G., and OLDFIELD, E., 1991, *Biochemistry*, **30**, 2333.

[101] MA, J., HUO, S., and STRAUB, J. E., 1997, *J. Am. chem. Soc.*, **119**, 2541.

[102] DLOTT, D. D., FAYER, M. D., HILL, J. R., RELLA, C. W., SUSLICK, K. S., and ZIEGLER, C. J., 1996, *J. Am. chem. Soc.*, **118**, 7853.

[103] MANI, S., PAULY, J., CONOLLY, S., MEYER, C., and NISHIMURA, D., 1997, *Magn. Reson. Med.*, **37**, 898.

[104] YANG, X., and JELINSKI, L. W., 1995, *J. Mag. Reson.* B, **107**, 1.

[105] RAHMELOW, K., and HÜBNER, W., 1997, *Appl. Spectrosc.*, **51**, 160.

[106] ELLIOT, A., and AMBROSE, E. J., 1950, *Nature*, **165**, 921.

[107] SAARINEN, P. E., 1997, *Appl. Spectrosc.*, **51**, 188.

[108] WILSON, E. B., JR, DECIUS, J. C., and CROSS, P. C., 1955, *Molecular Vibrations: The Theory of Infrared and Raman Vibrational Spectra* (New York: McGraw-Hill).

[109] ZIMDARS, D. A., 1996, PhD thesis, Stanford University.

[110] AUSTIN, R. H., BEESON, K., EISENSTEIN, L., FRAUENFELDER, H., GUNSALUS, I. C., and MARSHAL, V. P., 1974, *Phys. Rev. Lett.*, **32**, 403.